CHEMISTRY OF MATERIALS

Article

A new quasicrystal approximant in the Sc–Pd system: from topological data mining to the bench

Pavlo Solokha, Roman A. Eremin, Tilmann Leisegang, Davide M. Proserpio, Tatiana Akhmetshina, Albina Gurskaya, Adriana Saccone, and Serena De Negri

Chem. Mater., **Just Accepted Manuscript** • DOI: 10.1021/acs.chemmater.9b03767 • Publication Date (Web): 15 Jan 2020

A new quasicrystal approximant in the Sc–Pd system: from topological data mining to the bench

Pavlo Solokha[1*], Roman A. Eremin[2, 3], Tilmann Leisegang[2, 4], Davide M. Proserpio[2, 5], Tatiana Akhmetshina[2, 3], Albina Gurskaya[2, 3], Adriana Saccone[1], Serena De Negri[1]

[1] Università degli Studi di Genova, Dipartimento di Chimica e Chimica Industriale, Via Dodecaneso 31, I-16146 Genova, Italy

[2] Samara Center for Theoretical Materials Science (SCTMS), Samara State Technical University, Molodogvardeyskaya St. 244, Samara 443100, Russia

[3] Samara Center for Theoretical Materials Science (SCTMS), Samara University, Ac. Pavlov St. 1, Samara 443011, Russia

[4] Institute of Experimental Physics, TU Bergakademie Freiberg, Leipziger Str. 23, 09599 Freiberg, Germany

[5] Università degli Studi di Milano, Dipartimento di Chimica, Via Golgi 19, 20133 Milano, Italy

ABSTRACT: Intermetallics contribute significantly to our current demand for high-performance functional materials. However, understanding their chemistry is still an open and debated topic, especially for complex compounds such as approximants and quasicrystals. In this work, targeted topological data mining succeeded in (i) selecting all known Mackay-type approximants, (ii) uncovering the most important geometrical and chemical factors involved in their formation, and (iii) guiding the experimental work to obtain a new binary Sc–Pd 1/1 approximant for icosahedral quasicrystals containing the desired cluster. Single crystal X-ray diffraction data analysis supplemented by electron density reconstruction using the maximum entropy method, showed fine structural peculiarities, *i.e.* smeared electron densities in correspondence to some crystallographic sites. These characteristics have been studied through a comprehensive DFT modeling based on the combination of point defects such as vacancies and substitutions. It was confirmed that the structural disorder occurs in the shell enveloping the classical Mackay cluster, so that the real structure can be viewed as an assemblage of slightly different, locally ordered, four shell nanoclusters. Results obtained here open up broader perspectives for machine learning with the aim of designing novel materials in the fruitful field of quasicrystals and their approximants. This might become an alternative and/or complementary way to the electronic pseudogap tuning, often used before explorative synthesis.

INTRODUCTION

Chemistry of intermetallics is still one of the most complicated topics in materials science, mainly due to their strong and almost continuous variation with the composition and nature of the elements involved. Compounds formed by two or more metals exhibit a wide structural diversity, which is the origin of many difficulties in their description and classification. According to the crystallographic data analysis of Dshemuchadse & Steurer[1], among 20,829 intermetallics (involving 81 elements of the periodic table) crystallizing in 2,166 different structure types, almost 2% of the structures exhibit more than 100 atoms per unit cell and are therefore termed "complex intermetallics" (CIMs).

At the early stage, many CIMs were described as a packing of clusters and so-called "glue atoms" that fill the voids in between. The convenience and logic of the cluster representation of complex structures is obvious: intermetallics with more than a thousand[2,3] or even tens of thousands[4,5] of atoms per unit cell look much simpler when represented as cluster assemblages. Nonetheless, the physical significance of such a description, as well as the definition of the clusters themselves[6] still remain open questions.

Icosahedral quasicrystals (iQC) and their approximant crystals (AC) are classic examples of a numerous family of CIMs for which concentric shell-like (or nested) clusters are fundamental building units. Commonly, three topologically different structural fragments are distinguished among these, namely, Bergman-[7], Tsai-[8] and Mackay-type[9] clusters.

Under the assumption that a rhombic triacontahedron (RTH, 32 vertices) cluster is the principal building unit for the iQC $YbCd_{5.7}$, a successful structure solution could be realized in 2007[8]. An elegant generalizing scheme was then proposed for the periodic ACs of the iQCs: it was shown that the majority of Bergman- and Tsai-type rational ACs could share their RTH rhombic faces when *b*-linked or partially overlap if they were *c*-linked[10]. Recent studies for Tsai-type ACs have shown that both types of linkage can be successfully modelled by considering the formation of smaller clusters in the first step of crystal growth from the melt and further coalescence of remaining atoms "welding" them together[11]. The consideration of RTH as a structural unit not only significantly simplifies the ACs

representation, but also allows to avoid the use of "glue" atoms – a conventional but vague term describing the intercluster space[12]. It is worth noting that Mackay ACs were generally less considered in the framework of RTH simplification, mainly due to a deep disorder of their outer concentric shells[13]. On the other hand, disorder phenomena are quite common in the intermetallics realm and may appear in terms of distortions, strains, substitutional disorder[14–16], vacancy formation[17–20], stacking faults, intergrowth of different phases[21], or their combinations[22]. Although consequences of the defect presence in a structure can be experimentally detected, their detailed study is still quite challenging[17,21,22].

Notwithstanding the above-mentioned clusters were individuated as a clear structural descriptor for periodic ACs of the iQCs, they have not yet been exploited for the theoretical prediction of new approximants. This is likely due to their 3D periodic unit cell complexity, which is aggravated by a compositional disorder, resulting in an extremely high computational cost for theoretical methods like density functional theory (DFT). On the other hand, the most frequently used theoretical approaches to crystal structure prediction are based on purely geometric considerations, which are supplemented by evolutionary algorithms[23,24], without considering significant crystal chemical aspects.

In this work the scope of new approximant design was faced starting from the cluster-based description. Thus, graph theory was applied to perform meaningful data mining of the inorganic crystal structure database (ICSD) to find all known approximants containing Mackay clusters. Correlation diagrams were created and analysed with the aim of identifying key features for the existence of targeted compounds.

A major part of this article describes the synthesis and the comprehensive crystal and electronic structure analysis of a new orthorhombic 1/1 AC found in the Sc–Pd system, chemically related to those selected after topological data mining. For this off-stoichiometry compound, an intrinsic structural disorder was revealed, which was the origin of its detailed DFT-based modelling. A dense set of structural models with different compositions due to different defect fractions has been generated and relaxed. The convex hull thermodynamic criterion was used to evaluate the most stable configurations. From this experimental and theoretical study, a sound, consistent, and comprehensive interpretation of the crystal structure of the new AC was obtained with implications for the future search for other ACs.

2. Materials and Methods

2.1. Topological analysis – a useful starting point for data mining

The complex task of searching for CIMs that contain a certain finite fragment could take advantage of a tool that is independent of group theory. For example, graph theory can be helpful and topological methods can be used for raw data mining and targeted search for different structure classes[25–28]. The practice shows that this path reduces complexity of the subsequent investigations and, therefore, saves computational/experimental resources. In this work, the main attention is paid to a rational Mackay AC search within the entire Inorganic Crystal Structure Database (ICSD, release 2018_2; about 220,000 crystal structures), as earlier only a part of its entries was analysed[29]. The algorithm for selection and subsequent analysis of icosahedral Mackay-type ACs relies entirely on the procedures implemented in the ToposPro package[30] and includes the following steps:

(i) Calculation of the adjacency matrices[31] for all the crystal structures using the *AutoCN* program. Since the intermetallics belonging to the ACs family have highly coordinated crystallographic sites, all the significant interatomic contacts can be characterized by a certain set of faces of atomic Voronoi polyhedra (a threshold solid angle of 0.19 rad was chosen). As a result, 3D periodic nets were obtained for the entire database. More details on the adjacency matrix calculation and related criteria are reported in[31].

(ii) Application of a very fast and robust automated search algorithm properly adapted to a finite fragment (graph) of any complexity. The latter is generated in a text format depicting the shell graph of a 1@12@42 Mackay cluster. At the end, a complete list of compounds containing the template fragment was generated (see "Mackay cluster containing CIM.xlsx" in Supplementary Material).

(iii) Selection of the ACs from the list using several filters, such as the appropriate unit cell dimension range, the presence of "glue" atoms, and the relative disposition of Mackay clusters (they should not overlap) within the crystal structure as the most important ones.

(iv) Simplified representation of each AC structure in terms of underlying net topology: only the centres of gravity of Mackay clusters are considered preserving the global net connectivity.

(v) Finally, by applying the topological analysis described elsewhere[29,32], the underlying building patterns have been classified according to the Reticular Chemistry Structure Resource nomenclature[33] and ToposPro databases[34].

2.2. Synthesis, SEM-EDXS and DTA

To obtain the title 1/1 AC phase, mixtures of pure Sc pieces and Pd foil (more than 99.9% purity, MaTecK, Jülich, Germany) with $Sc_{74}Pd_{26}$ and $Sc_{80}Pd_{20}$ nominal compositions and with a total weight of 0.6 g were melted three times in an arc furnace under Ar atmosphere. A simple recrystallisation cycle was applied to the $Sc_{80}Pd_{20}$ alloy to obtain good quality single crystals. The as-cast sample was enclosed in a tantalum crucible and then in an

evacuated quartz phial to prevent oxidation and finally placed in a resistance furnace. It was heated up to 1150 °C (10 °C/min) and subsequently slowly cooled down (–0.2 °C/min) to room temperature (RT).

A Zeiss Evo 40 (Carl Zeiss SMT Ltd.) scanning electron microscope (SEM) coupled with a Pentafet Link Energy Dispersive X-ray Spectroscopy (EDXS) system managed by INCA Energy software (Oxford Instruments, Analytical Ltd.) was used for microstructure observation and crystallographic phase analysis. Figure S1 of the Supplementary Material shows the micrographs of $Sc_{74}Pd_{26}$ and $Sc_{80}Pd_{20}$ samples: the former contains Sc_2Pd as primary crystals together with the 1/1 AC phase, the latter shows as major (>90%) phase the target 1/1 AC with only small amounts of elemental Sc. In both alloys, the semi-quantitative elemental composition for 1/1 AC grains is ~78 at. % Sc and ~22 at. % Pd.

Differential thermal analysis (DTA) was performed for the $Sc_{80}Pd_{20}$ alloy to confirm the type and temperature of formation reaction for the 1/1 AC, as already presented in the published Sc-Pd phase diagram[35] (the phase of interest there is called ~Sc_4Pd, see Figure S2a). The measurement was carried out using the LABSYS EVO (SETARAM Instrumentation) analyser equipped with type-S Pt-PtRh 10% thermocouples, in the temperature range from 25 to 1050 °C, and a homemade tantalum crucible. An empty tantalum crucible was used as reference. The DTA curve was recorded under a continuous argon flow (20 mL/min) according to the following cycle: RT → 1050 °C (10°C/min; 10 min plateau) → RT (–10 °C/min). The obtained thermogram was elaborated with the Calisto software supplied by SETARAM. The sample was characterized by SEM/EDXS prior and after the DTA experiment. It was confirmed that the 1/1 AC forms peritectically at *ca*. 980 °C (see Figure S2b).

2.3. Single crystal X-ray diffraction and electron density reconstruction

Small crystals with metallic lustre (further indicated as *crystal I* and *II*) were carefully selected from the fragmented $Sc_{80}Pd_{20}$ alloy, glued on glass fibres and positioned into a Bruker Kappa APEXII diffractometer equipped with a molybdenum X-ray tube. Data was recorded using ω-scans at ambient conditions. Data integration, Lorentz polarization, and semiempirical absorption corrections were applied to all data by using the SAINT and SADABS software[36]. Crystal structures refinements were carried out by full-matrix least-squares methods on $|F|^2$ using the SHELXL program[37] as implemented in WinGx[38]. The corresponding CIF files, available as supplementary material, have been deposited at Cambridge Structural Database with the following depository numbers: CSD-1874074 (*crystal I*) and CSD-1874073 (*crystal II*). Details on the structure solution are discussed in Section 3.2.

For the reconstruction of the electron density (ED), the model-independent Maximum Entropy Method (MEM) was used as implemented in the BayMEM program package[39]. The experimental structure amplitudes *F*(obs) were processed with the crystallographic computing system Jana2006[40]. The PRIOR program was used for the prior calculation using the structure parameters from the independent spherical atom model (ISAM) refinement of the $Sc_{56}Pd_{15}$ (*Immm*, *oI*142, *Z* = 2). Subsequently, the EDMA program was used for the quantitative characterization of the EDs, *i.e.* atomic coordinates, atom charges, and volumes according to the quantum theory of atoms in molecules (QTAIM)[41]. Selected crystallographic data, structure refinement parameters, and details on the ED reconstruction are given in Table S1.

2.4. Compositional/configurational spaces sampling

The structural models generated for compositional/configurational space sampling were derived from the idealized (ordered) $Sc_{56}Pd_{15}$ model (*Immm*, *oI*142, *Z* = 2). In order to achieve relevant off-stoichiometry structure models, two types of possible point defects were considered: "vacancy" (empty crystallographic site) and "substitution" (substitution of one atom sort by another one). As will be shown below, this is enough to describe the structural peculiarities observed by X-ray diffraction and within corresponding ED maps (Sec. 3.3).

Two compositional/configurational spaces were set by using the Supercell program[42], which provides *P*1 symmetry representations of the disordered structures, necessary for DFT modelling. Firstly, model unit cells with single point defects (vacancy or substitution) in every crystallographic site were generated (a schematic representation of the applied procedure is given in Figure S6 of Supplementary Materials). Since there are 18 occupied Wyckoff sites for the $Sc_{56}Pd_{15}$ structure, the irreducible "Single Defect Compositional/Configurational Space" (SDCCS) contains 36 (18 for vacancies and 18 for substitutions) symmetrically inequivalent entries (*cf.* steps 1.1–1.3 in Figure S6 of Supplementary Materials). Secondly, the defect formation energies of SDCCS were calculated by means of DFT and the energetically favoured point defects on different crystallographic sites were identified. After that, a "Combined Defect Compositional/Configurational Space" (CDCCS) aimed at investigation of the thermodynamic properties of highly disordered structures was constructed combining in various quantities the point defects on the selected sites.

To keep a reasonable computational complexity of the subsequent DFT calculations for CDCCS, the combined point defects generation was performed only for two crystallographic positions: Sc9 (4*f*) and Sc12 (8*m*) (*cf.* Table 1). These sites show the lowest defect formation energies for the averaged vacancy and substitution contribution. Considering the maximum number of point defects on each disordered site equal to 4 (limit, sufficient for

modelling conducted here), more than 200 independent structure models arise. Even within such a simplified approach, due to the high multiplicities of the selected Wyckoff sites, the resulting complexity of the irreducible CDCCS with more than 17,000 entries lies beyond the reasonable limits. Therefore, a reduced number (1,041 entries) of independent configurations for each unique combination of point defects was randomly selected and relaxed within DFT.

One more structural model of hypothetical $Sc_{57}Pd_{13}$ 1/1 AC constructed by analogy with related compounds[43] (see "Mackay cluster containing CIM.xlsx" in Supplementary Materials) was also considered for DFT calculations to explore its thermodynamic properties in the Sc–Pd system. Additionally, for the most energetically favoured entries of the studied CDCCS, a number of structural models containing vacancies and substitutions on the Pd5 (4*j*) site (this site is also affected by disorder from X-ray diffraction point of view) were set and calculated by means of DFT.

2.5. DFT calculations

The obtained structures of SDCCS and CDCCS were relaxed using the DFT approach implemented in the *Vienna Ab Initio Simulation Package*[44]. The projector-augmented wave method[45] and the generalized gradient approach were used with Perdew-Burke-Ernzerhof (PBE) exchange-correlation functional[46]. The recommended pseudopotentials (Sc_sv: $3s^2 3p^6 4s^2 3d^1$, Pd: $4d^9 5s^1$) were selected. The energy cutoff value of 600 eV was set. For binary intermetallics, structure relaxation runs were carried out at the *Γ*-point of the reciprocal space. For pure metals, the reciprocal space sampling was done within the *Γ*-centered Monkhorst-Pack scheme (Sc: 5×5×3, Pd: 4×4×4). For comparison of the theoretical and experimental results, the atom charges were calculated according to QTAIM[41].

According to the compositional/configurational space sampling described above, the introduction of a discrete amount of point defects should lead to crystal symmetry reduction. For this reason, any constraints during a structure/cell optimization were switched off. The convergence control parameters for total energy and maximum force acting on an ion were set to 10^{-4} eV and 10^{-3} eV/Å, respectively.

For a certain A_xB_y configuration with the characteristic energy of $E_{A_xB_y}$, the formation energy per atom E_f was calculated by using formula (1), where E_A and E_B are the characteristic energies per atom of the *A* and *B* constituents in a pure metal state, respectively:

$$E_f = \frac{E_{A_xB_y} - xE_A - yE_B}{x + y} \quad (1)$$

To conclude whether a configuration is thermodynamically stable, the convex hull approach[23,47] was applied. For this purpose, a reference E_f line (hull) linking Sc_2Pd, ordered $Sc_{56}Pd_{15}$, and Sc was constructed covering the whole compositional range of the generated models. The SDCCS models showing the minimum formation energies with respect to the hull (E_{hull}) were considered for further generation of the CDCCS entries. After their DFT relaxation, the convex hull was recalculated with reference to the new E_f values of the more thermodynamically stable compositions. In accordance to this, the E_{hull} values for the SDCCS entries are given related to the first mentioned hull (Sc_2Pd–$Sc_{56}Pd_{15}$–Sc) and serve for the selection of the promising "defect" sites, whereas the E_{hull} values for the CDCCS configurations are evaluated with respect to the updated hull.

Density of States (DOS) comparative analysis between the initially X-ray guessed structure ($Sc_{56}Pd_{15}$) and the energetically most favoured one after CDCCS exploration ($Sc_{55}Pd_{16}$) was performed. An enhanced sampling of the reciprocal space (*k*-mesh of 12×12×12 leading to 510 irreducible points) was applied to the pre-relaxed configurations within the all electron, full-potential local orbital method (FPLO, version 9.00)[48]. The PBE exchange and correlation functional was used, considering also scalar relativistic effects.

2.6. Parameters used for ACs' maps construction

The necessity of a critical evaluation of the most common factors used for structure maps construction arose through their application to the group of Mackay type ACs found by topological data mining. Independently from the number of elements, each of these compounds can be considered as composed of species acting as cations (major constituents) and others acting as anions. Thus, the following parameters were chosen:

(a) *Volume contraction*: it is the relative volume change passing from the elements to the intermetallic compound introduced by Merlo[49] and defined as $\Delta V_f(\%) = 100 \times (V_{calc} - V_{meas})/V_{calc}$, where $V_{calc} = \sum_i N_i \times V_i$, ($N_i$ is the number of *i*-type atoms in the unit cell, V_i the atomic volume of the *i*-type species taken from Ref. [50]) and V_{meas} is the experimentally determined volume taken from the ICSD.

(b) *Electron count*: the electron concentration for each AC was calculated according to the formula: $(e/a)_{AC} = [\sum_i N_i \times (e/a)_i]/N$, where $(e/a)_i$ is the electron concentration for each atomic species, according to Ref. [51] and *N* is the total number of atoms in the unit cell.

(c) *Effective atomic size ratio*: the effective atomic size ratio $R_{r,e}$ proposed by Tsai[10] was adjusted according to the following formula: $R_{r,e} = \sum_a (r_a \times N_a)/\sum_c (r_c \times N_c)$, where r_a, r_c are the atomic radii of anions and cations[52] and N_a, N_c, are their number in the unit cell, respectively.

(d) *Electronegativity difference*: the formula of the Martynov-Batsanov electronegativity difference ($\Delta\chi$) taken from Ref. [53] was adapted to obtain the mean difference of electronegativities: $\Delta\overline{\chi} = 2 \times \sum_a N_a \times (\sum_a \chi_a - \sum_c \chi_c)/N$, where χ_a, χ_c are the Martynov-Batsanov electronegativity values for the anion and cation, respectively[54].

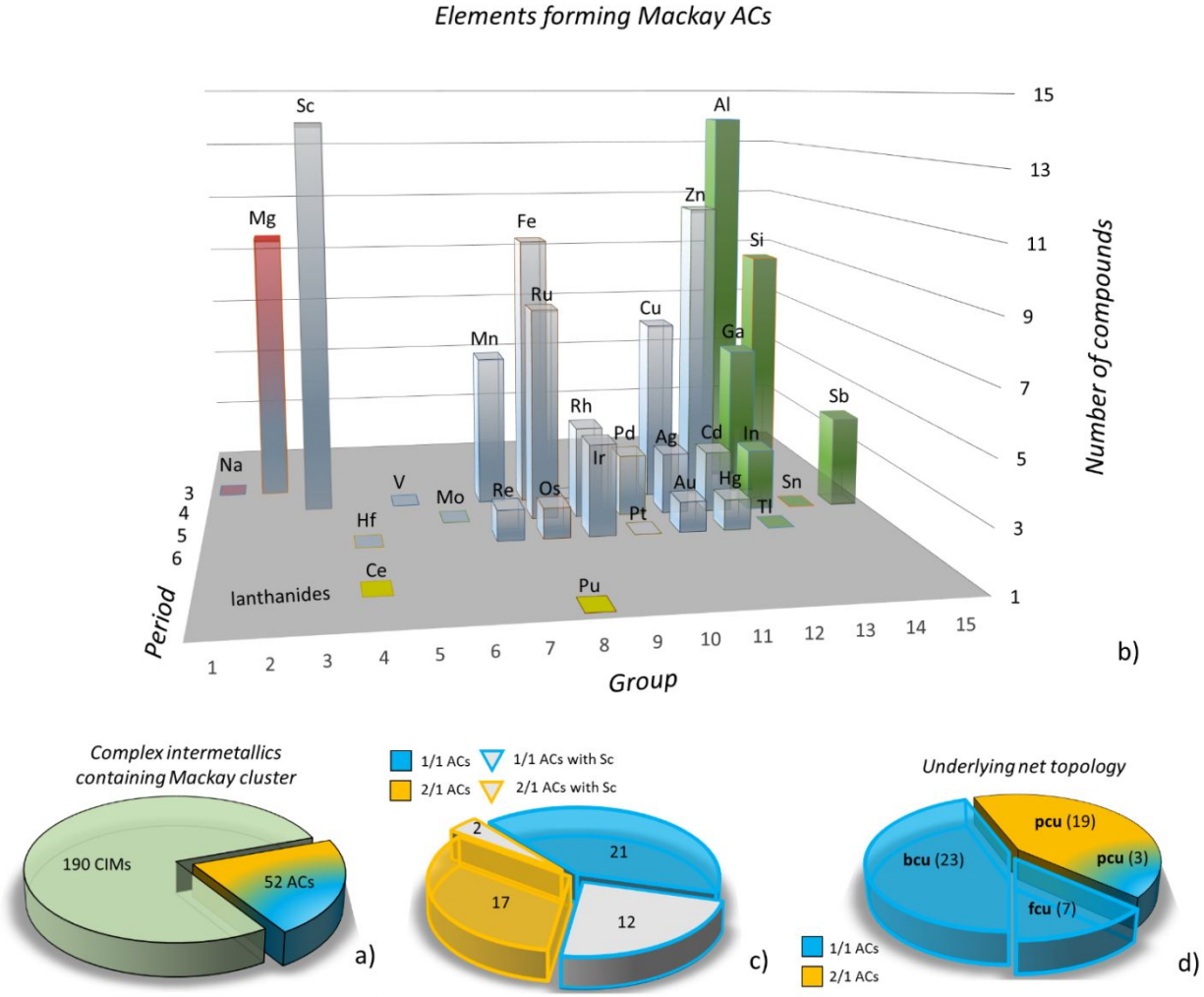

Figure 1. Statistics of Mackay-type ACs discovered up to date: a) fraction of ACs among CIMs containing Mackay clusters; b) distribution of elements forming the 52 ACs of Mackay type; c) Sc distribution among 1/1 and 2/1 ACs; d) characteristic underlying net topology of the Mackay cluster assemblages for the found ACs. Blue and yellow filler/borders for pie charts are associated to 1/1 and 2/1 ACs, respectively.

3. Results and discussions

3.1. Rational Mackay ACs known up to date

When this investigation had been started on occasion of Alan Mackay's 90th birthday[29] a curiosity arose – how one can find a group of compounds with a certain structure characteristic such as a Mackay-type cluster within ever-growing databases? Statistical data elaboration based on symmetry properties, such as space group, Pearson symbol, lattice parameters and standardized representations[55] may help to some extent[1], but it is also known that among intermetallics, frequently, structural relations exist between chemically different systems with different number of atoms in the unit cell, different sets of Wyckoff sequences and different space groups. The Hume-Rothery (HR) phases and ACs offer numerous examples of that[56–58].

Using the algorithm described in Sec. 2.1, a total of 242 intermetallics containing the Mackay cluster as a finite graph were found. Among them, 52 ACs were recognized (see Figure 1a): 24 binary, 23 ternary and 5 quaternary compounds (the complete list of 52 ACs can be found in "list of ACs.xlsx" in Supplementary Materials section). Among this ACs group, 33 compounds are of 1/1 and 19 of 2/1 type (see Figure 1c; for a detailed description of structural peculiarities of q/r rational ACs the reader is referred to[59]).

As follows from the element distribution plot shown in Figure 1b, the late transition metals frequently appear. With rare exceptions, the active metal (see Lin *et al.*[60]) in

all the compounds is Sc, Mg, Zn or Al, mainly present as the principal component (> 50 at. %).

From the structural point of view, all the selected ACs can be viewed as simple packings of Mackay-type nanoclusters well known as base-centered cubic (**bcu**), face-centered cubic (**fcu**) and primitive cubic (**pcu**[33]). Whereas the 1/1 ACs may possess any of the mentioned topologies, the 2/1 ACs are always characterized by the **pcu** network (see distribution in Figure 1d).

The performed topological data mining provided also a valuable shortcut for the synthesis of novel ACs/QCs, highlighting a compositional playground to be explored. In this study, attention was focused on the Sc-rich group of ACs (14 compounds, mainly binaries, 12 of 1/1- and 2 of 2/1-type, see Figure 1c and Table S2).

At this point, the Sc–Pd binary system was selected for experimental investigation considering different aspects:

- palladium is a coin metal, chemically related to other transition elements forming ACs with Sc;

- from the literature, the existence of the ~Sc_4Pd phase is already known,[35] for which no structural model has been proposed;

- the theoretical high-throughput first-principles calculations performed[47] did not reveal any stable compound in the Sc-rich region;

- from the structural point of view, Sc–Pd is an excellent combination due to the good X-ray scattering contrast of constituents.

3.2. Crystal structure of "$Sc_{56}Pd_{15}$" 1/1 AC from ISAM and MEM refinements

The indexing of the *crystal I* diffraction pattern results in an orthorhombic body-centered Bravais lattice with a = 14.27 Å, b = 14.37 Å, c = 14.79 Å. No additional systematic extinction conditions were identified for this dataset. The initial structure model was determined to belong to the centrosymmetric *Immm* (71) space group using the charge flipping algorithm implemented in Jana2006[40]. The unit cell contains 142 atoms distributed among 5 Pd and 13 Sc independent Wyckoff sites, giving the $Sc_{56}Pd_{15}$ composition. The obtained model is isopointal with the known $Hf_{54}Os_{17}$ structure type[43]; the different stoichiometry between them is due to the Os 4*f* site (0.20 1/2 0), which is occupied by Sc in our case. This model showed similar isotropic thermal displacement parameters U_{eq} for all sites except for those of Sc9 and Sc13 that were 2–3 times larger. In order to improve the structure model, the occupancy parameters of all the crystallographic sites were varied in a separate series of least squares cycles along with the displacement parameters. They did not significantly deviate from full occupancy and were assumed to be unity in further cycles. However, the R factors dropped significantly when anisotropic thermal displacement parameters (ADP) were introduced. It turned out that the thermal ellipsoids of only Sc9 and Sc13 sites are highly distorted, being stretched along the edges of the triangular face they form (see Figure S3 in Supplementary Materials). Moreover, several strong peaks were present in the difference Fourier map located too close to Sc13 and Sc9 sites to be considered fully occupied. In the final structure model, these sites were considered for refinement as split Sc13/Sc23/Sc33 (constraining their total occupancy to 100%) and partially substituted Sc9/Pd9 (the SIMU[61] command was used to refine their ADPs). The refinement converged to comparably good residuals of R_1 = 0.03, wR_2 = 0.06 and *GOF* = 1.09 complemented by a flat difference Fourier map with residual electron densities lower than 2 e/Å^3 (see Table S1).

With the purpose to check whether such a disordering is an intrinsic feature of the studied specimen, one more single crystal (*crystal II*) was selected and subjected to XRD. It turned out that this crystal exhibits the same distortions of the ADPs and splitting-like character for Sc9 and Sc13 sites.

The structure models obtained for *crystals I* and *II* are similar within the standard deviations of 3σ (*e.g.*, the atomic coordinates deviate by less than 1%) and are reported in Table 1 and Table S3 (Supplementary Material), respectively. The refined composition of both crystals matches well the measured ones (SEM-EDXS results; see Supplementary Material) and only slightly deviates between each other: $Sc_{55.44}Pd_{15.54}$ and $Sc_{54.98}Pd_{15.56}$.

It is worth noting that several different scenarios describing the unusual behaviour of Sc9 and Sc13 sites were tested (*e.g.* Sc13-Sc23/Pd13-Pd23 mixed sites with no occupational restriction; split Sc9 site; partially occupied Pd9 site) giving no noticeable improvement of the residuals. This fact, however, affects the assigning of the correct chemical composition of the studied phase from the structural data and shall be addressed in more detail with the subsequently applied MEM and DFT modelling.

In our opinion, the most convenient and intuitive way of describing the crystal structure of the studied AC is in terms of a short-range (SRO) and a long-range order (LRO) of constituting clusters. This scheme was repeatedly used for elucidation of the crystal structures of mainly Bergman- and Tsai-type rational approximants[10,62]. SRO defines the type of AC and reflects its endohedral shells radial ordering. In our case, the Pd1 is located in the centre of the cluster, followed by a Sc_{12} icosahedron (Sc1, Sc4, Sc5 sites). The second shell is defined by a Sc_{30} icosidodecahedron (Sc2, Sc3, Sc6, Sc8, Sc10, Sc11 sites) followed by the third shell in form of a Pd_{12} icosahedron (Pd2, Pd3, Pd4 sites). The mentioned shells constitute a classical (55 atoms) centred Mackay cluster, depicted in Figure 2.

Table 1. ISAM and MEM standardized structural data[55] as well as effective charges Q_{eff} (determined after Bader atomic population subtraction from atomic number) and Bader volumes deduced from MEM and DFT for crystal I. Analogous data for crystal II can be found in Table S3 of Supplementary Materials.

Space group: *Immm* (71), Pearson symbol-prototype: *oI*142-1.01, $Hf_{54}Os_{17}$, lattice parameters: a = 14.2681(7), b = 14.3696(7), c = 14.7848(7) Å												
ISAM						MEM					DFT*	
Atom–Wyck. site	*x*/*a*	*y*/*b*	*z*/*c*	SOF ≠ 1	U_{eq} (Å²)	*x*/*a*	*y*/*b*	*z*/*c*	Q_{eff} (e)	Bader vol. (Å³)	Q_{eff} (e)	Bader vol. (Å³)
Pd1–2*a*	0	0	0		0.0091(1)	0	0	0	−0.9	26.6	−2.8	33.9
Pd2–8*n*	0.33560(2)	0.20626(2)	0		0.0118(1)	0.33566	0.20601	0	−1.3	27.3	−2.8	35.4
Pd3–8*l*	0	0.33423(2)	0.21002(2)		0.0128(1)	0	0.33447	0.21024	−0.3	26.1	−2.6	33.7
Pd4–8*m*	0.20347(2)	0	0.33362(2)		0.0131(1)	0.20329	0	0.33375	−0.7	25.4	−2.9	36.3
Pd5–4*j*	1/2	0	0.16129(3)		0.0162(1)	1/2	0	0.16169	+1.8**	22.2**	−2.2	31.2
Sc1–8*n*	0.17841(5)	0.10944(5)	0		0.0092(1)	0.17880	0.10949	0	+0.8	14.1	+0.4	19.6
Sc2–4*i*	0	0	0.35361(7)		0.0094(2)	0	0	0.35312	+0.4	18.5	+0.4	21.0
Sc3–4*e*	0.38016(7)	0	0		0.0095(2)	0.38052	0	0	+1.0	14.8	+1.3	14.5
Sc4–8*l*	0	0.18171(5)	0.10583(5)		0.0091(1)	0	0.18344	0.10601	+0.4	15.5	+0.7	17.4
Sc5–8*m*	0.11011(5)	0	0.16815(5)		0.0091(1)	0.10995	0	0.16849	+0.7	14.1	−0.5	26.8
Sc6–16*o*	0.11696(4)	0.17771(4)	0.28718(3)		0.0100(1)	0.11693	0.17790	0.28748	+0.6	17.2	+0.7	18.7
Sc7–8*l*	0	0.32341(6)	0.39631(5)		0.0125(1)	0	0.32337	0.39649	+0.6	17.0	+1.2	14.1
Sc8–4*g*	0	0.37974(8)	0		0.0108(2)	0	0.38008	0	+0.8	17.9	+1.0	17.5
Sc9–4*f*	0.1857(11)	1/2	0	0.49(4)	0.016(2)	0.20308	1/2	0	−0.5**	18.5**	+0.1	23.1
Pd9–4*f*	0.2251(11)	1/2	0	0.26(2)	0.025(2)							
Sc10–16*o*	0.18707(4)	0.30113(4)	0.11127(4)		0.011(1)	0.18727	0.30123	0.11095	+0.3	19.7	+0.9	17.1
Sc11–16*o*	0.30196(4)	0.11509(4)	0.17770(4)		0.010(1)	0.30213	0.11542	0.17788	+0.6	16.7	+1.0	16.2
Sc12–8*m*	0.39766(6)	0	0.32996(6)		0.017(1)	0.39808	0	0.33	+0.7	15.5	+0.9	15.9
Sc13–8*n*	0.3878(12)	0.3792(11)	0	0.44(3)	0.012(4)	0.39124	0.37862	0	+0.6	19.0	+0.7	18.5
Sc23–8*n*	0.367(2)	0.3938(17)	0	0.27(3)	0.013(3)							
Sc33–8*n*	0.4093(17)	0.370(2)	0	0.29(3)	0.010(2)							
Refinement details: GOF = 1.1; independent reflections: 2550; R_{int} = 0.032; R_1/wR_1 = 0.028/0.029; $\Delta\rho_{res}$ (max./min.) = 1.6/-2.0 (e/Å³)***												

*The listed values were obtained for the ordered $Sc_{56}Pd_{15}$ structure model, with Sc9 and Sc13 fully occupied (see text).

**These values reflect the disorder at this site and are not necessarily reasonable.

***Further details are summarized in Table S1 of the Supplementary Material.

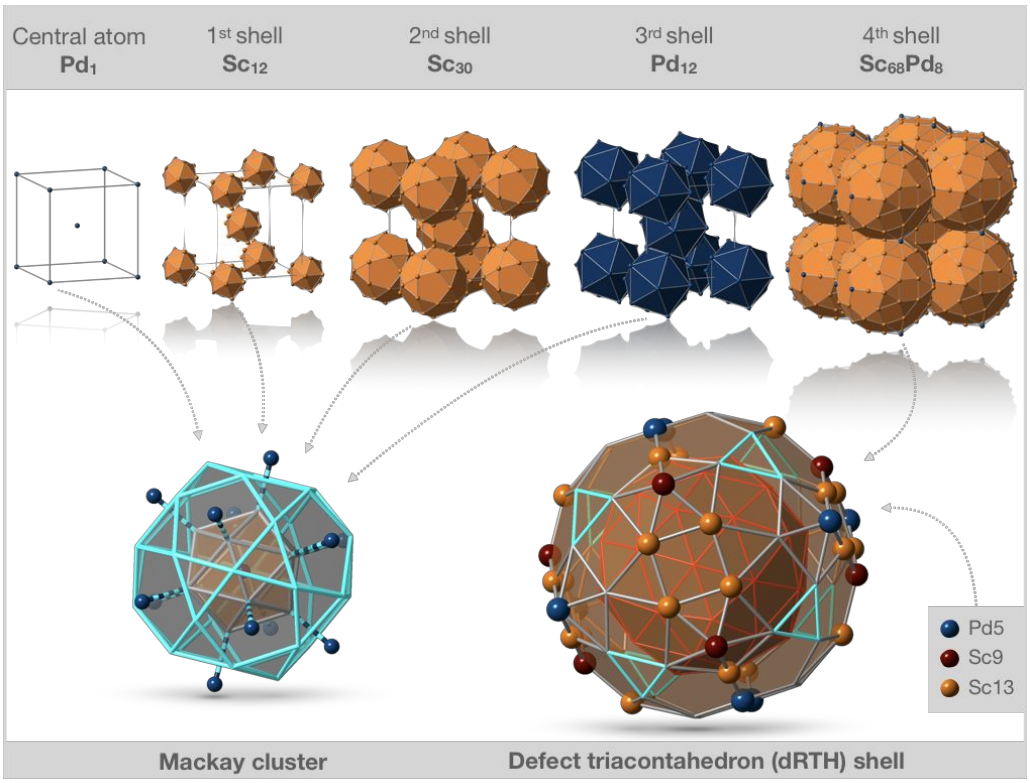

Figure 2. Short-range order, *i. e.* hierarchy of the four endohedral shells of the Mackay nanocluster in the ~$Sc_{56}Pd_{15}$ 1/1 AC, which are arranged concentrically around the central Pd atom (top row). The centred Mackay cluster (bottom) consists of a Sc_{12} icosahedron (1st shell, grey edges), Sc_{30} icosidodecahedron (2nd shell, turquoise edges) and Pd_{12} outer icosahedron (3rd shell, the vertices of which are connected to the inner ones by dashed lines). The $Sc_{68}Pd_8$ defect triacontahedron (bottom; 4th shell, grey and turquoise edges) encloses the Mackay cluster (now with the Pd_{12} shell; red lines). For reasons of clarity, the inter-shell bonds are not shown and only the characteristic atoms Pd5, Sc9 and Sc13 (*cf.* Table 1) are shown. These are regarded here as unique, fully occupied positions. Clusters and structures were visualized with CrystalMakerX[63].

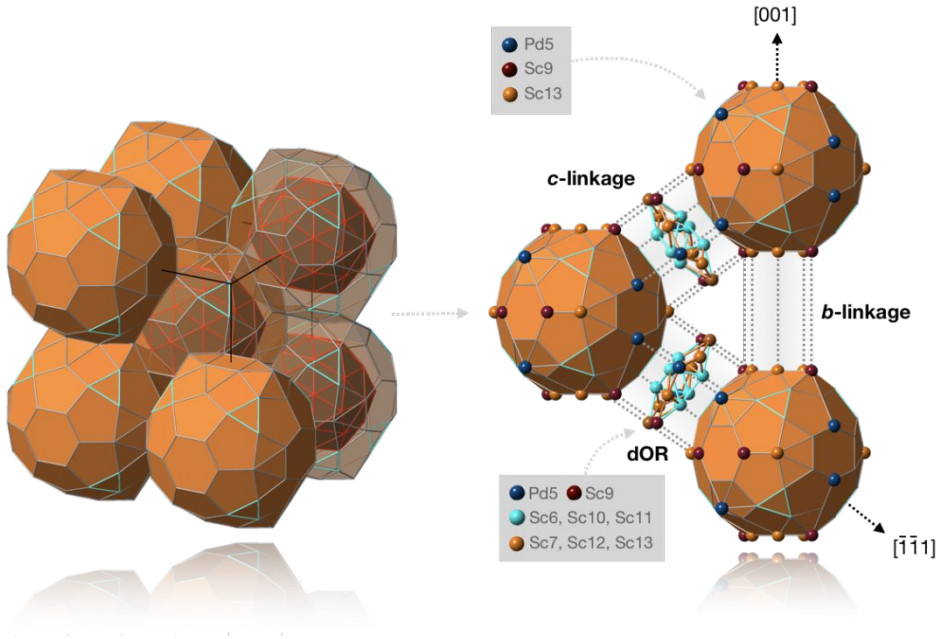

Figure 3. Long-range order and schematic representation of the base-centred packing of dRTH for the 1/1 AC together with *b*- and *c*-linkage of two adjacent dRTH. Note that a *c*-linkage of two dRTH along the <111> direction implies the formation of defect oblate rhombohedra (dOR), which are shown separately.

With the purpose to avoid the presence of "glue" atoms in the outer limits of the principal Mackay cluster, one more external shell was considered with $Sc_{68}Pd_8$ composition (see Figure 2), that could be defined as a defect rhombic triacontahedron (dRTH (16v, 60e)) with 16 vertices less with respect to the commonly adopted undistorted edge decorated RTH (32v, 60e). The independent crystallographic sites Sc7, Sc9, Sc12, Sc13 and Pd5 exclusively belong to this shell whereas Sc6, Sc10 and Sc11 (linked by turquoise solid line in Figure 2) constitute also in part the inner icosidodecahedron.

In total, the SRO defined nanocluster consists of 131 atoms. A simple base-centered packing of dRTH-topology clusters describes the LRO of the title approximant (see Figure 3). It is worth recalling that an identical type of RTH clusters' packing was already proposed for 1/1 Bergman and Tsai ACs[60]. Thus, we may conclude that the LRO principle is the same for different 1/1 ACs. The *b*- and *c*-linkage of dRTH clusters along the basic lattice vectors and the <111> diagonal direction, respectively, are also evidenced in Figure 3. The *b*-linkage implies sharing of rhombohedral edges between neighbouring dRTH; instead, a defect oblate rhombohedron (dOR) of $Sc_{14}Pd_2$ composition is formed between two dRTH when *c*-linked.

The comparison of interatomic distances with tabulated data of 3.20 Å, 3.00 Å and 2.80 Å for Sc–Sc, Sc–Pd and Pd–Pd contacts, respectively, in fact, supports the structure description in terms of nanocluster assembly:

Sc atoms within the first icosahedral shell are distanced at *ca*. 3.1 Å. For the second shell, the distances slightly increase ranging from 3.1 to 3.4 Å. Obviously, since the atoms are placed on a sphere of bigger radius, they suffer less geometrical strains. Sc–Sc interactions within the dRTH shell are in a similar range: Sc9 and Sc13 atoms are involved, among others, in the shortened (2.86 Å) or excessively elongated (3.67 Å) homoatomic interactions. This might be considered as an indication of some structural hindrances, which are addressed in more details below. Interestingly, the intershell Sc–Sc contacts are similar to those in elemental Sc.

Pd atoms location within the nanocluster reflects their tendency to maximize the number of hetero contacts. They are surrounded by only Sc atoms inside the Mackay cluster. The Pd3–Pd5 contacts, occurring at the periphery, exceed the atomic radii sum. A pronounced shortening is manifested by Sc–Pd interactions (2.7 to 2.9 Å) holding together different shells. The Pd5 located in the dRTH shell is also strongly linked to the neighbouring Sc species.

To visualize the structural peculiarities, the ED was reconstructed. Figure 4 shows the shell hierarchy of the Mackay-type nanocluster in terms of the classical description and volumetric MEM-EDs together with the (001) ED section at $z = 0$ delimiting the outer dRTH shell. The atoms belonging to the inner (1st – 3rd) shells show sharp distinct spherical ED distributions, whereas atoms exhibiting strong distortions are located exclusively in the dRTH shell (see also Supplementary Material, Figure S4).

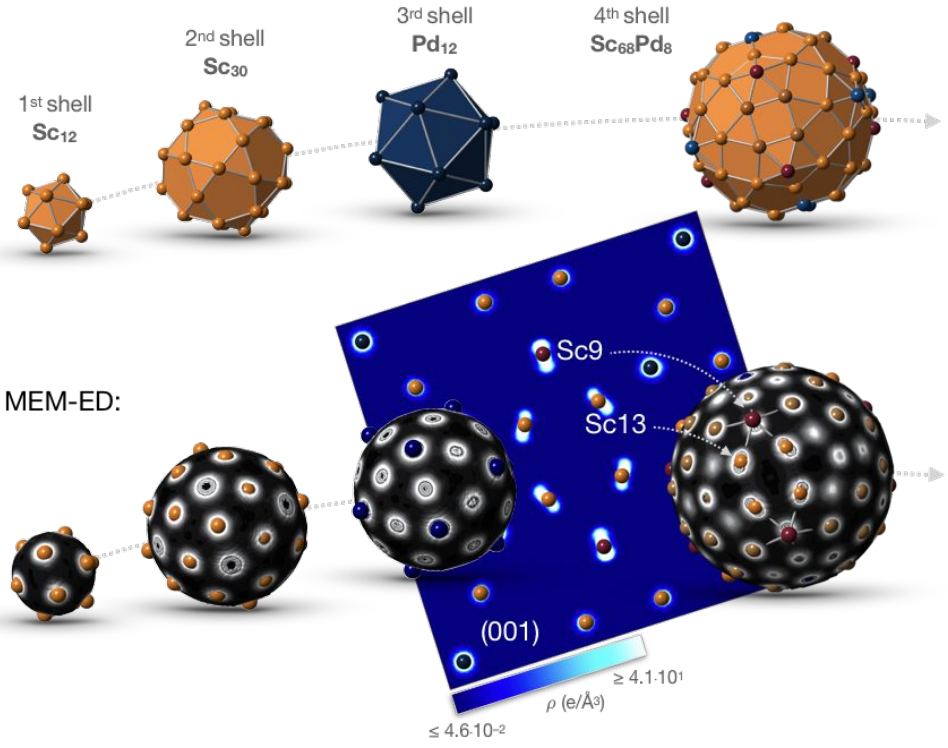

Figure 4. The 131 atoms nanocluster as a concentric arrangement of the four considered shells. The top shows a schematic representation, while the bottom shows the overlaid ED. The (001) section of the ED at z = 0 is shown in the background. The Sc9 and Sc13 atoms are exclusively labeled since they are characterized by elongated ADPs and strongly non-spherical ED distributions.

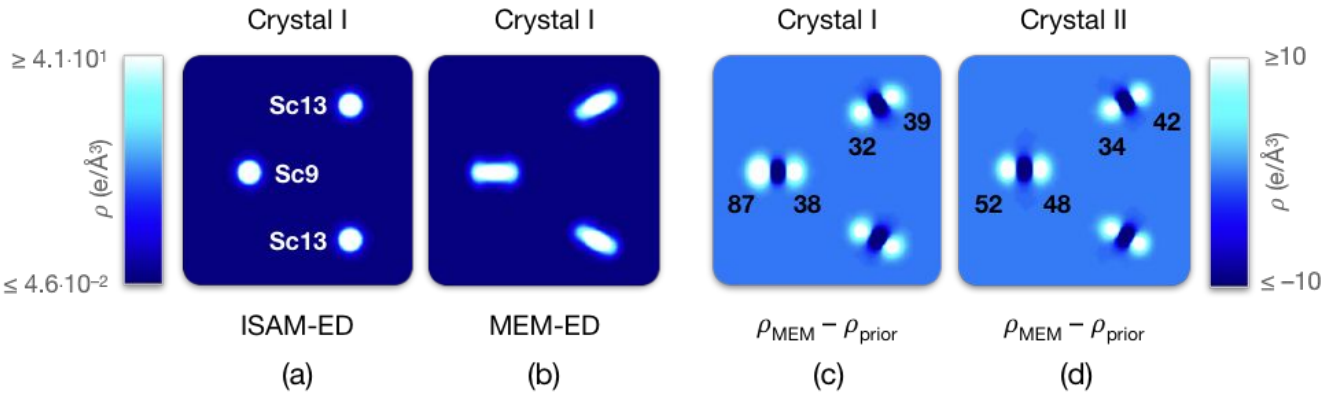

Figure 5. Representation of ISAM (a) and MEM (b) ED of the (001) partial section at z = 0 including positions Sc9 and Sc13. The difference EDs for *crystal I* (c) and *crystal II* (d) have two strong maxima in the vicinity of each mid-position characterized by different heights (numbers are given in e/Å³).

Figures 5a–b visualize the characteristic ED distribution of Sc9 and Sc13 atoms within the (001) ED and difference ED sections at z = 0 derived from ISAM and MEM. A quantitative evaluation of the difference ED for both investigated crystals shows two strong and not equal maxima next to each central position (Figures 5c–d). In fact, the two spatially divided maxima corresponding to Sc9 are considerably different in ED values (87 e/Å³ *vs.* 38 e/Å³) for crystal I, whereas those of crystal II are nearly similar (52 e/Å³ *vs.* 48 e/Å³). On the other hand, for the Sc13 site, the difference ED is more symmetrical, and the two maxima stay in a similar proportion for both crystals. Such a distribution is too pronounced to be associated with chemical bonding effects and points at a specific structural disorder.

In order to give a deeper insight on that, a comparative analysis between the effective atomic charges (Q_{eff}) obtained from MEM experimental data and those calculated for the DFT-relaxed defect-free $Sc_{56}Pd_{15}$ was performed (see Table 1 and Figure 6).

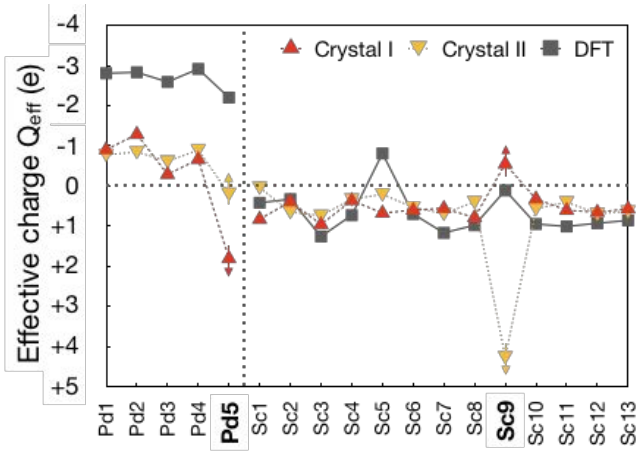

Figure 6. Experimental (ISAM/MEM) and theoretical (DFT) effective charges of the atoms. The dotted lines are a guide for the eye; arrows highlight the out-of-trend behavior of Pd5 and Sc9 atoms.

Considering their noticeably different Martynov-Batsanov electronegativities,[54] Sc (χ = 1.5) and Pd (χ = 2.08) are expected to act as cation and anion, respectively. In line with this observation, the DFT data listed in Table 1 confirm that all Pd atoms possess negative charges: Pd1, Pd2, and Pd4 have only Sc atoms as nearest neighbours (at distances of about 2.6 Å) and therefore show lower charges with respect to Pd3 and Pd5 being distanced at 3.1 Å. Sc atoms generally show positive charges although varying between +0.126 and +1.256 whereas Sc5 represents a noticeable exception, being negatively charged (see Figure S5). This fact is unexpected because Sc5, Sc1, and Sc4 constitute the inner icosahedron and possess the same coordination sphere in form of a bicapped pentagonal prism of $Sc@Sc_{10}Pd_2$ composition with similar interatomic distances. Nevertheless, if one considers the interactions along the line starting at the Pd central atom and passing through Sc5, Sc1, Sc4 and further versus the nanocluster limit, the number/types of the interacting atoms are, in fact, different. We believe that this might be responsible for the unusual Sc5 behaviour and its enlarged atomic basin.

Compared with DFT data, the MEM Q_{eff} values follow the same general trend (Figure 6), however, chemically unreasonable values for Pd5 and Sc9 strike the eye. Most likely this is due to the observed disorder. It has to be noted that DFT values may deviate from MEM mainly because DFT does not consider thermal motion, uses periodic boundary conditions that do not consider real-structure effects, and the partitioning of the ED may suffer from spurious basins that are not considered by the atomic charge integration procedure in EDMA.

Considering the observed distorted ED, *i.e.* point defects, neither MEM nor DFT approach can give a fully adequate representation of QTAIM characteristics. To shed light on the role of the point defects for the studied off-stoichiometric 1/1 AC, a DFT screening of the compositional/configurational spaces was performed.

3.3. Tuning the 1/1 AC's composition with DFT

3.3.1. Energy balance: single point defects disordering

In this section the robustness of the 1/1 AC crystal structure against structural defects such as vacancies and substitutions (one Pd atom on Sc site and *vice versa*) is examined. As reference energy we consider the part of the convex hull that encloses the formation energies of Sc-rich phases, *i.e.* Sc_2Pd–$Sc_{56}Pd_{15}$–Sc. For the SDCCS entries, the E_{hull} values serve as a measure of the vacancy and substitution formation energies and are plotted in Figure 7 (the numerical values are listed in Table S4; Figure S6 of Supplementary Materials gives a detailed explanation of SDCCS sampling).

As can be seen from Figure 7, increasing the distance of the considered site from central Pd1 promotes the formation of defect on it. The first two shells of the Mackay cluster are the most "vacancy resistant" shells: the energetic costs of vacancy formation actually vary from 13 meV/atom to 20 meV/atom from Sc5 to Sc3. Far from the center, within the third and fourth endohedral shells, the formation of vacancies is more likely: the E_{hull} tends to decrease, resulting in the lowest value of 1 meV/atom for the Sc9 position.

The local minimum for the Sc11 site deserves a more detailed explanation. It has been found that while DFT structure relaxation, a Sc atom shifts its location from the Sc12 site, which is characterized by a low vacancy formation energy, to the Sc11 site. Thus, the (pseudo) low vacancy formation energy on the Sc11 site actually represents the vacancy formation energy on the Sc12 site.

The substitution defect formation energies show the same tendency: the corresponding E_{hull} increases from 8 meV/atom to 15 meV/atom from Sc5 to Sc3, followed by a decrease to −2.1 meV/atom for the Sc9 site. Local maxima (*e.g.* for Sc3, Sc7, and Sc13) can be explained by considering Coulomb interactions: the presence of Pd at these sites increases electrostatic repulsion with other negatively charged Pd atoms in their first coordination sphere. For the same reasons, several Sc positions such as Sc5, Sc1, Sc4, *etc.* have similar substitution defect energies (*cf.* Figure 7).

From the above discussion it becomes clear that starting from the central atom substitutions are initially more favoured (from Pd1 to Sc8), then the formation of defects of both types (from Pd2 to Sc9) competes, whereby the fourth shell is the preferred one for disordering phenomena. This observation is consistent with the structural trends observed in Tsai-type clusters: the atomic positions of the inner shell are less affected by chemical disorder but instead the RTH sites are susceptible to mixed occupancies[58].

Among the 36 SDCCS studied defect structures, the presence of Pd on Sc9 leads to a negative E_{hull} value of −2.1 meV/atom, indicating that this is the most favourable scenario.

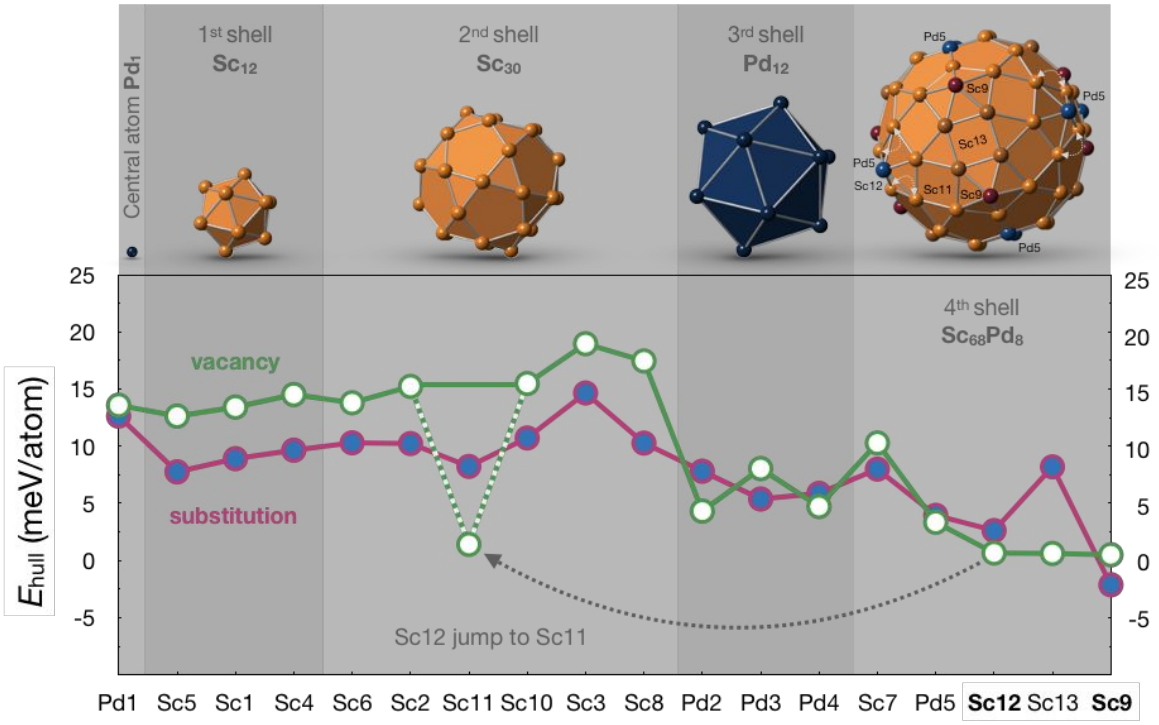

Figure 7. E_{hull} calculated by DFT for the SDCCS entries. The crystallographic sites are ordered in relation to their distance from the center of the Mackay cluster and grouped by the four characteristic shells. The local minimum for the Sc11 site is indicated by green dashed lines (see text for details). The sites in bold are further considered for disorder phenomena studies.

The vacancy formation on that position corresponds to the second lowest E_{hull} value of 0.5 meV/atom, which reinforces the notion that this site is the most affine to disorder. The vacancy formation on Sc12 and Sc13 has an almost similar influence on the SDCCS energy balance (E_{hull} values of 0.7 meV/atom and 0.6 meV/atom, respectively). However, the substitution for Sc12 is energetically more advantageous compared to Sc13 (2.6 meV/atom *vs*. 8.2 meV/atom). At this stage of the analysis we can conclude that the vacancy/substitution within the 4th shell is a reasonable mechanism for the observed off-stoichiometry. Therefore, the Sc9 (4*f*) and Sc12 (8*m*) sites were selected for the next stage of the study, taking into account the combination of both types of defects (CDCCS).

The unique Pd site located on the dRTH shell (Pd5) shows the third lowest mean defect formation energy as well as positive effective charge of the MEM. It would therefore be advisable to include it in the subsequent CDCCS studies. However, this would have drastically increased the cost of calculation, which is why the relaxation and formation energy calculations were only performed for a limited number of defect configurations at this site. The configurations chosen for further defect modelling on Pd5 were the most energetically favoured after CDCCS for Sc9 and Sc12 (see next section).

3.3.2. Energy balance: combined defects disordering

Due to the high CDCCS complexity, the number of admitted point defects within the same crystallographic site was limited to 4, which was sufficient to consistently describe the experimental findings. Thus, the maximum defect fractions for the chosen Sc9 (4*f*) and Sc12 (8*m*) sites are equal to 1 and 1/2, respectively. Looking at the Sc9 disorder alone, the maximum amount of each type of point defects would correspond to independent structure models with the fully vacant or fully Pd-substituted 4*f* site, each resulting in a single CDCCS entry. The other structure models describe the configurations with all possible combinations of fractions of vacancies (*FV*), substitutions (*FS*), and remaining Sc atoms (*FR*) on this site ($FV + FS = 1 - FR$), which may have more than one low-symmetry realization. For a more detailed explanation, see the CDCCS sample flowchart in the Supplementary Materials.

There are 225 structural models for the defined maximum number of defects (4 + 4) that occur at the two selected crystallographic sites (*cf*. step 2.1 in Figure S6). The complete CDCCS for such a combined disordering consists of 137,457 entries (*cf*. step 2.2 in Figure S6). Due to the symmetry equivalence of some low-symmetry (down to *P*1) structure representations within a given structure model, the complete CDCCS can be minimized to a set of symmetrically inequivalent representations, *i.e.* irreducible CDCCS (*cf*. step 2.3 in Figure S6). In our case, a total of 17,739 configurations constitute the irreducible CDCCS. In order to reduce the complexity of the DFT calculation, an additional criterion was defined: for each independent structure model, a maximum of five different low-symmetry configurations was randomly selected. In this way, only 1,041 CDCCS entries remain.

The formation energies of all DFT-optimized configurations compared to their Sc content are shown in Figure 8a. For reasons of clarity, the CDCCS entries are divided into two groups: (*i*) CDCCS part which is not influenced by random selection (red circles) and (*ii*) CDCCS part which is represented by 5 random structures (grey crosses). It is noteworthy that group (*i*) contains a number of configurations describing Sc9 disordering with a small amount of Sc12 defects ($FV + FS \leq 1 - 7/8$) whose formation energies are close to the convex hull; this is in good agreement with the results of the SDCCS modelling.

The four modes of defect distributions (vacancies and substitutions at Sc9 and Sc12 sites) and the estimated formation energies define a five-dimensional CDCCS description. 3D representations thereof, limited to the thermodynamically most stable ($E_{hull} < 5$meV/atom) CDCCS entries, are shown in Figure 8b and 8c. For example, each column in Figure *8*b corresponds to a certain number of the low-energy CDCCS entries with a certain *FS*/*FV* on Sc9 and various disorder combinations on Sc12. According to Figure 8c, each defect on Sc12 is unfavourable, which is in excellent agreement with the experimental observations; the substitutions are even less favourable than the vacancies. At zero defect content on Sc12 there are a number of low energy configurations due to defects on Sc9. On the other hand, it can be inferred from Figure 8b that the substitution scenario on Sc9 corresponds to several energetically favoured CDCCS entries. The following description of the results therefor concerns CDCCS entries with disorder only on Sc9.

Within the Sc_2Pd–Sc range, the energetically preferred configuration is $Sc_{55}Pd_{16}$ (space group *Imm*2; Sc9 site occupied by 2 Pd and 2 Sc atoms; complete structural data are listed in Table S5 in Supplementary Materials). From the energy point of view, numerous CDCCS entries are located near the updated Sc_2Pd–$Sc_{55}Pd_{16}$–Sc convex hull. It is worth noting that for the models located in the narrow concentration range of ~2 at.% between $Sc_{54}Pd_{17}$ (E_{hull} = 0.7 meV/atom; Sc9 site occupied by 4 Pd atoms) and the initial $Sc_{56}Pd_{15}$ (E_{hull} = 2.6 meV/atom; Sc9 site completely occupied by scandium), there is a small difference in formation energy costs.

The complete sets of values of total energies, formation energies, and E_{hull} values corresponding to both the Sc_2Pd–$Sc_{56}Pd_{15}$–Sc ("*E*hull, meV/atom" column) and the newly defined Sc_2Pd–$Sc_{55}Pd_{16}$–Sc ("Ehull2, meV/atom" column) convex hulls are contained in the additional file "SUPPL-Sc56Pd15.xlsx" as Supplementary Material. An alternative representation of the 1,041 E_{hull} values *vs.* defect fractions on Sc9 and Sc12 is shown in Figure S7.

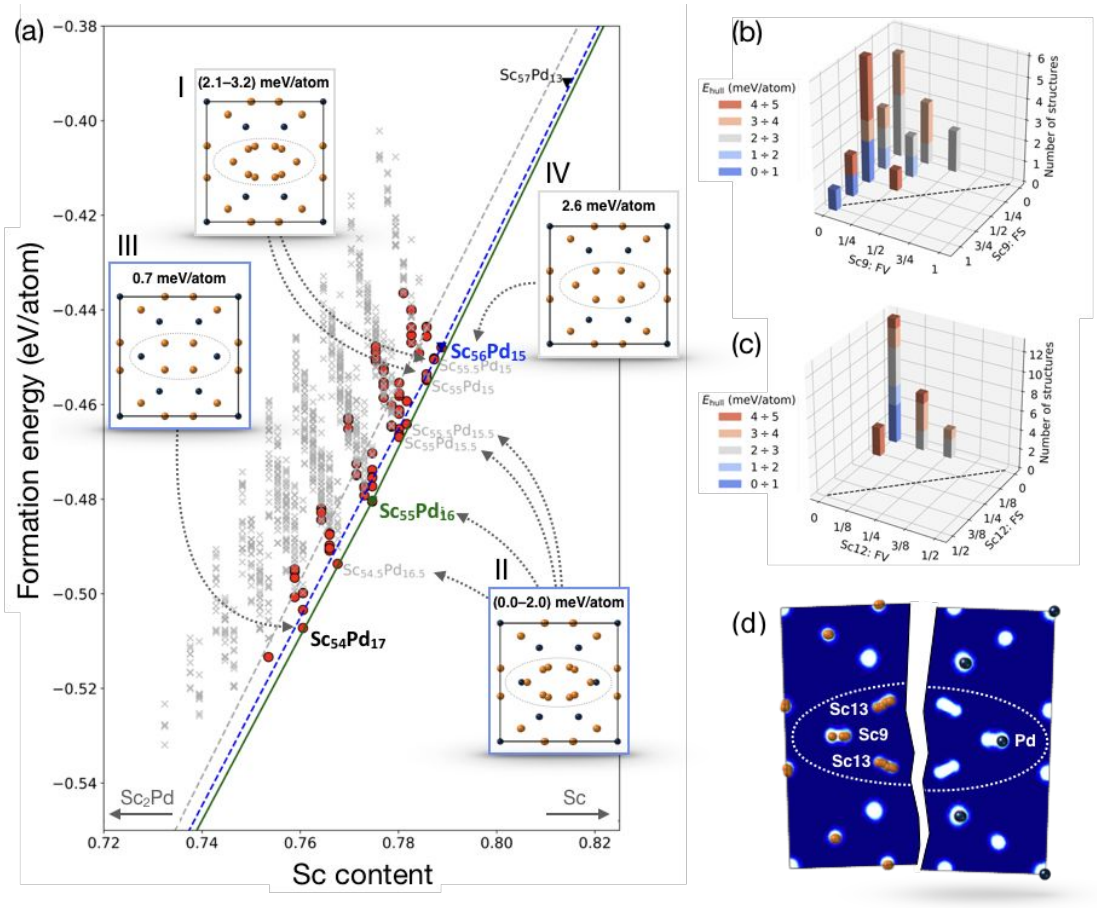

Figure 8. (a) Formation energies of the CDCCS entries versus Sc content together with the Sc_2Pd–Sc (gray dashed line), Sc_2Pd–$Sc_{56}Pd_{15}$–Sc (blue dashed line) and Sc_2Pd–$Sc_{55}Pd_{16}$–Sc (green solid line) convex hulls. The CDCCS entries are divided into two groups: (i) not affected by the random criterion (red circles) and (ii) randomly reduced configuration sets (gray crosses). The (001) planes obtained after applying the *Immm* space group symmetry operations are displayed as insets I – IV for selected structural models (see text for details); (b) and (c) E_{hull} values (with respect to the Sc_2Pd–$Sc_{55}Pd_{16}$–Sc convex hull) for the energetically preferred structures compared to mixed defect concentrations with fixed FS/FV on Sc9 (b) and Sc12 (c) sites; (d) partial ED sections overlaid with all merged and symmetrized CDCCS entries with E_{hull} < 2.6 meV/atom, indicating a perfect agreement between the modeling results and the experimental ED in correspondence to Sc9 and Sc13 sites (details in the text). For reasons of clarity, the atomic positions derived from the merged models are disjoint into the two species Sc (left) and Pd (right). In all structure projections ellipses serve as a guide for the eye and mark the area in which the most remarkable structural changes occur.

Another interesting point is that the hypothetical cubic binary compound of $Sc_{57}Pd_{13}$ stoichiometry (*cI*140, $Im\bar{3}$, $Sc_{57}Rh_{13}$ prototype), which was tested together with CDCCS, was found slightly above the refined convex hull (3.9 meV/atom) (Figure *8*a), in accordance with the fact that this compound was not found under the experimental conditions assumed here. Deeper investigations are necessary on the existence of $Sc_{57}Pd_{13}$ as a metastable or high temperature phase.

3.3.3. Comparison of theoretical models with experimental data

According to the CDCCS modelling, the formation energies of numerous compositionally close structural models differ by only a few meV/atom. Therefore, the influence of the synthesis conditions could be decisive to determine which model(s) are obtained in the experiment. On the other hand, it is also difficult to obtain clear experimental evidence for the realized scenario. First, because defects in real crystals are thermodynamically favoured and different defects can be realized at the same time. Second, the limits also result from the resolution of the experimental methods. For example, the ubiquitous, fast, and widely available semi-quantitative electron probe micro analysis is inefficient to distinguish the concentrations of very similar compounds, which in our case differ by less than 2 at.%. TEM, spectroscopy, X-ray and electron diffraction are also unable to distinguish such

subtle structural distortions. For these reasons, the case under investigation blurs the differences between the classical definitions of "point compound" and "solid solution" and offers the need to reflect about a more general approach.

Despite the drawbacks indicated above, we undertake to compare the modelling results with the experimental findings. Differences between the two crystals (see ISAM and MEM results for Sc9 site) may be intrinsic or due to the different methods used.

In order to perform a qualitative comparison, (001) cross-sections were calculated for the energetically favoured CDCCS entries after their merging under restoration of the symmetry conditions of *Immm* space group (insets of Figure 8a). Their analysis shows that the introduction of a defect on Sc9 position induces the virtual formation of a spatially split Sc13 position. The introduction of only vacancies is sufficient to obtain configurations such as $Sc_{55}Pd_{15}$ (2.1 meV/atom; 2 Sc and 2 vacancies) and $Sc_{55.5}Pd_{15}$ (3.2 meV/atom; 3 Sc and 1 vacancy), as shown in Figure 8a inset I.

More relevant are models that contain only one substitution or the combination of substitution and vacancy on Sc9 (including the $Sc_{55}Pd_{16}$ composition). Four of these models have a similar effect on the averaged structure (inset II of Figure 8a): in addition to the already mentioned virtual split Sc13 site, a virtual spatial split of Sc9/Pd9 position also becomes apparent. These are $Sc_{55.5}Pd_{15.5}$ (3 Sc and 1 Pd atoms), $Sc_{55}Pd_{15.5}$ (2 Sc, 1 Pd, and 1 vacancy), $Sc_{55}Pd_{16}$ (2 Sc and 2 Pd atoms) and $Sc_{54.5}Pd_{16.5}$ (1 Sc and 3 Pd atoms).

These observations obviously explain the apparent experimental ED distributions shown in Figure 5, asymmetric for Sc9 and almost symmetrical for Sc13. The excellent correspondence between the models described and the experimental data can be seen in Figure 8d, where all the symmetrized CDCCS entries were merged with the lowest E_{hull} values (< 2.6 meV/atom) and overlaid with the deduced ED.

In summary, the CDCCS sampling confirmed that the Sc9 site is the most affine to disorder, in accordance with the experimental data and the SDCCS results. Instead, disorder on the Sc12 site (proposed after SDCCS sampling) is of minor relevance, in accordance with the experiments. The most interesting conclusion is that the Sc13 site (virtually) splits as a consequence of disorder on the Sc9 site. This accounts for the observed ED distribution, although a compositional disorder on this site was not suggested by SDCCS. The selection of the most thermodynamically favourable models according to CDCCS is the best approximation to the real structure, which is not deducible by X-ray diffraction.

Finally, the Pd5 Q_{eff} values derived by the MEM outside the trend (see Figure 6) could be explained by a partial atomic substitution. The CDCCS models presented so far do not cover changes in composition on the Pd5 site. For this reason, additional DFT calculations have been performed. Based on $Sc_{55}Pd_{16}$, 40 further structure models were constructed in which the Pd5 site is occupied by one vacancy or Sc atom, characterized by E_{hull} values in the range of 3.3 meV/atom to 4.1 meV/atom. The further inclusion of point defects definitely increases E_{hull}. A more comprehensive investigation of the distribution of such defects would require supercells, which would greatly increase the computational time and complexity of CDCCS. Nevertheless, it can be suggested that defects at the Pd5 site are possible from the thermodynamic point of view and coherent with the experimental observations.

3.4. Traces of Hume-Rothery stabilization mechanism from the DOS for the Sc-rich 1/1 AC

It is known that a (deep) pseudogap at the Fermi level is associated with the stability of icosahedral clusters containing compounds such as QCs and their ACs or defect structures[64–67]. There are two principal interpretations of this: Hume-Rothery (HR) type stabilization with Fermi surface–Brillouin zone interactions or (*spd*) orbital-hybridizations. According to HR physics, the energy of the occupied electron states can be lowered by nesting of the Fermi sphere in a near-spherical Brillouin zone, leading to electron depletion at the Fermi energy. In contrast to covalently bonded compounds or ionic crystals, where local interactions lead to stable structures, the stabilization for the Hume-Rothery phases is of non-local origin. This is the case with iQCs belonging to HR phases[67] for which a nearly spherical Brillouin zone is characteristic.

The total DOS of the disorder-free X-ray-derived structure model of the studied compound ($Sc_{56}Pd_{15}$, *Immm*, *oI*142) and the energetically most favoured one after CDCCS exploration ($Sc_{55}Pd_{16}$, *Imm*2, *oI*142) are shown in Figure 9a. The negligible differences between the two curves are located well below the Fermi level (E_F) being associated with the different Pd content. Instead, almost identical DOS trends are observed in the vicinity of E_F. They indicate a metallic behaviour and are characterized by a pronounced, almost symmetrical pseudogap of ~0.8 eV. This indicates a HR-type stabilization mechanism as proposed for many ACs of iQCs.

The atom-projected, orbital-resolved partial DOS curves are shown in Figure 9b and 9c for $Sc_{55}Pd_{16}$. The chemical role of the constituents could easily be derived from their *d*-orbital contribution to the DOS: the low-lying *d*-orbitals of Pd are coherent with its high electronegativity, whereas those of Sc are predominant in the conduction band, in line with its cationic behaviour. Alike separation between the *d*-orbitals of the different species was observed for other binary HR phases, *i.e.* Cu_5Zn_8 (gamma brass), $CaCd_6$, and $ScZn_6$ (both Tsai-type 1/1 ACs)[51]. Similar orbital hybridization effects are also common for title binary ACs, which are described with respect to $Sc_{55}Pd_{16}$ (Figures 9b, c):

- the projected DOS suggests the contribution of different orbitals to pseudogap formation (see trends of *s*,

p, *d* states (Sc) and *p* states (Pd), for which bonding and antibonding sub-bands are well separated);

- noticeable orbital hybridizations derivable from the pDOS trend and the energy overlapping range occur between *s*(Sc)–*s*(Pd) and *p*(Sc)–*p*(Pd) states as well as between *s*, *p*(Pd) states, and the *d*(Sc) valence band, giving rise to the widely used term "*spd* hybridization". These features confirm the contribution of *s*, *p*, and *d* orbital mixing around E_F to the stabilization of ACs in addition to the Fermi sphere–Brillouin zone effects.

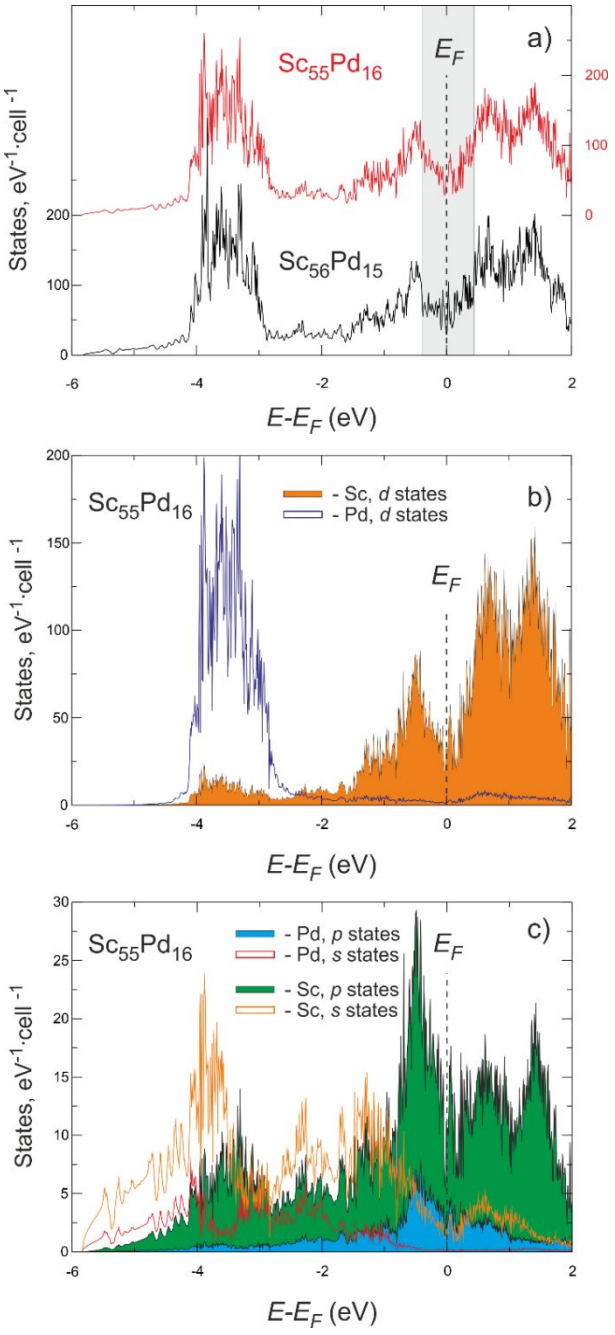

Figure 9. a) Total DOS curves for $Sc_{55}Pd_{16}$ (red line) and $Sc_{56}Pd_{15}$ (black line). The gray area highlights the pseudogap near E_F; b) and c) atom projected, orbital resolved partial DOS.

The striking DOS similarity for the selected binaries is an indication of a relationship between Tsai- and Mackay-type ACs that is worth exploring elsewhere.

As a conclusion of the discussion of the electronic structure, it should be mentioned that the pseudogap tuning by changing the chemical composition under the assumption of rigid band has frequently been used for the successful discovery of some new QC/AC systems[60,68,69]. However, several drawbacks of this chemical approach are evident: the rigid band assumption is often an over-simplification as it does not take into account that the phases before and after tuning are structurally different[60]; moreover, neither other phases actually compete with that of interest nor reaction conditions are considered.

The results obtained here after the CDCCS sampling demonstrate that the presence of a DOS pseudogap is not sufficient to deduce the best structural/compositional model in the chosen system. Instead, the thermodynamics is very helpful both for this purpose and to overcome the synthesis linked obstacles.

3.5. Geometrical vs chemical factors for Mackay ACs maps construction

Novel material design is a major goal of material science, linked to the fundamental question: which elements and how should they be combined to obtain a solid with the desired properties? Different phenomenological methods based on experimental observations aim at rationalizing known data as well as predicting unknown compounds/structures. These methods are rapidly evolving thanks to the general machine learning[70] approach, and take advantage of the ever-increasing computing power that makes it possible to process large amounts of data. In fact, meaningful data mining is the first step of a successful output for subsequent material design.

As part of this investigation, the Mackay cluster was imposed as a desired building block and an ICSD database screening based on this structure descriptor was performed (Sec. 2.1.). The group of 52 selected Mackay-type ACs has been extended by the new Sc-rich AC discovered here. At this point it is interesting analyse this set of compounds in terms of geometrical and chemical aspects commonly adopted by intermetallics' maps construction[54] (Sec. 2.6). It is known that ACs belong to the Hume-Rothery phases for which the electron concentration is proposed as an important factor governing their formation[10,60,71]. Therefore, here we consider the $(e/a)_{AC}$ parameter, which represents the average number of valence electrons per atom for each compound. Another important chemical factor is related to the electronegativities of the constituents. Among the numerous scales, Martynov-Batsanov's, which is conceived for crystalline inorganic compounds, was chosen; the corresponding $\Delta\overline{\chi}$ calculated for a compound, is linked both to the role and to the concentration of the constituents.

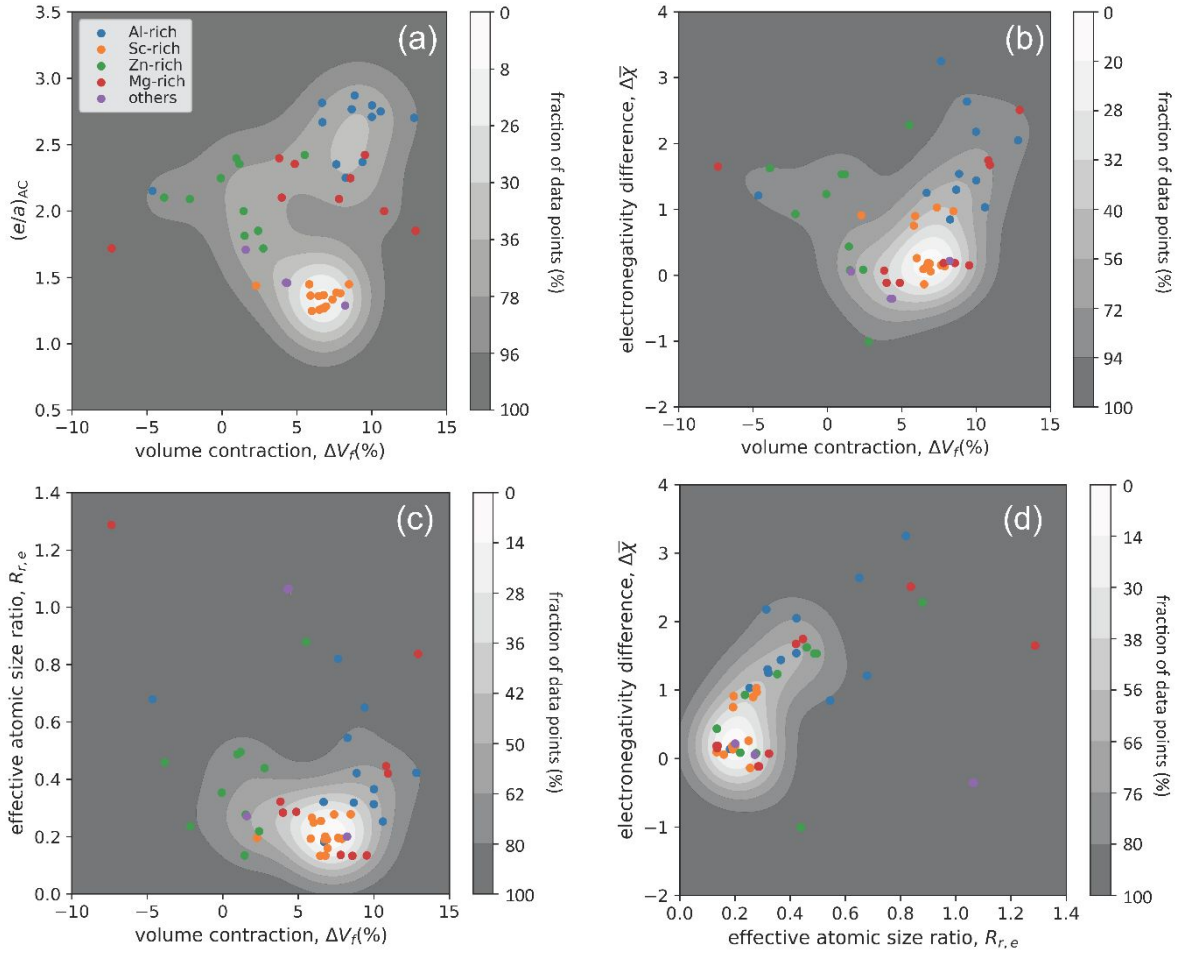

Figure 10. Point density maps representing the selected Mackay-type ACs distribution as a function of different parameters: average number of valence electrons per atom $(e/a)_{AC}$, volume contraction ΔV_f, electronegativity difference $\Delta\overline{\chi}$, and effective atomic size $R_{r,e}$. The grey-shaded areas represent increasing point densities from dark grey to white.-The cumulative percentage of data points is given on the right side of each figure.

Dimensional/geometric factors have also been proven to be efficient in separating different families of compounds. The effective atomic size ratio $R_{r,e}$ proposed by Tsai[10] specifically for ACs and iQCs, was adopted in this study taking into account the chemical role and concentration of the components.

In this way, two anion-rich compounds ($Ce_{77.68}Hg_{330.32}$ and $Pu_{77.68}Hg_{330.32}$) were discarded from the analysis as they have $R_{r,e}$ values significantly higher than others due to the inverse role of the elements. Finally, volume contraction ΔV_f (%) was chosen as a factor reflecting the combined influence of geometric and chemical effects[49]. A positive ΔV_f represents a contraction – the stronger the interactions, the stronger the volume contraction – while a negative ΔV_f represents an expansion.

Figure 10 represents different combinations of the four abovementioned parameters. A clear spatial separation for Al- and Sc-rich ACs can be observed along the $(e/a)_{AC}$ axis (Figure 10a), with Mg- and Zn-rich ACs distributed between them. This is an obvious consequence of using the same $(e/a)_i$ for each individual element and the fact that cation species dominate. It should be remembered that the $(e/a)_i$ values used were calculated by Mizutani[51] for each element taking into account its crystal structure and almost free electron behaviour. Although this approach is less arbitrary than others (such as Pauling and Raynor's) the resulting electron concentration represents unpolarized interactions in solids. In general, this situation is hardly feasible for compounds, in which polar interactions are always present. In our case we have a large chemical diversity of components in a number of structurally similar compounds for which the criterion of electron counting appears to be poorly efficient and would hardly be used for their design. In this context, the Zintl-Klemm concept should also be mentioned, in which a complete charge transfer is assumed and the structural distribution of atoms obeys the 8-*N* rule[72]. This concept is very useful, but in many cases does not work if only partial polarization occurs; an example has recently been discussed considering a family of polar ternary intermetallics[73].

The map shown in Figure 10b highlights that about 85 % of the compounds are localized in the range $0 < \Delta V_f$ (%) < 12 and $-0.7 < \Delta\overline{\chi} < 3$ without a clear separation depending on the main constituent. A similar situation can be seen in Figure 10c, d. The range of the effective atomic size ratio encompassing the majority of ACs is $0 < R_{r,e} < 0.8$.

In summary, it can be said that the maps produced here, which are based on geometric and electronegativity difference parameters, have proved to be efficient in grouping the investigated set of compounds. It should be noted that these are not classical structural maps that discriminate between different types of structures, but they allow connections to be made on the basis of similar structural motifs, validating topological data mining. Therefore, these correlation diagrams highlight the most probable regions of the existence of new Mackay approximants and related quasicrystals.

4. Conclusions

The manifold approaches applied in this study show that the topologically based screening is extremely useful in the design of new materials. Indeed, after a simple and fast automated procedure, a set of compounds containing the Mackay type cluster as a building block was selected from all the known inorganic crystalline solids and subsequently reduced to a subset of 52 rational ACs.

Simple **bcu**, **fcu** and **pcu** packings of multi-shell nanoclusters already proposed for these compounds are easily deducible for the selected ACs using the applied procedure. The topologically selected family is an excellent playground for further phenomenological approaches to identify the most important factors governing the formation of these types of materials. The constructed maps showed that combinations of geometric factors such as volume contraction and effective atomic ratio together with the mean electronegativity difference can be considered as excellent guiding criteria for planning the synthesis of new such materials.

In fact, the Sc–Pd system was chosen as the target for the discovery of new ACs and an orthorhombic 1/1 Sc-rich AC was successfully obtained. Single crystal X-ray diffraction data analysis performed with both ISAM and MEM approaches revealed fine structural peculiarities – smeared EDs of some crystallographic sites associated with the outer dRTH shell of the Mackay nanocluster. These features made it difficult to derive an unambiguous structural model with a given composition.

With the aim of obtaining the most reliable structure model, a compositional/configurational space sampling starting from the "raw" X-ray structure was performed. To the best of our knowledge, this is the first attempt to perform this type of modelling for such a structurally complex compound: a number of structure models were generated that cover a narrow concentration range and combine different quantities of vacancies and substitutions within the external dRTH shell. In order to compare the thermodynamic stability of the generated configurations, the convex hull approach was applied. As a result, several compositionally close (<1 at. %) models with negligible differences in formation energies were found, so that their relative thermodynamic stability could easily be influenced by temperature effects. Astonishingly, merging these by fixing the symmetry elements as revealed by X-ray diffraction, the average situation is perfectly consistent with the experimental observation. The determined disordered structure can be considered as derived from an assemblage of slightly different, nevertheless locally ordered fragments (nanoclusters). In other words, it can be described as slight short-range "disorder" under the condition of a long-range order, that in turn causes the X-ray diffraction. This conclusion is consistent with the structural features of other ACs that exhibit a disorder frequently affecting the most external nanocluster shell. On the other hand, this supports the idea of a two-stage crystallization from the melt[11], which has found several experimental evidences for iQC containing alloys[74–76].

The characterization of the new 1/1 Mackay AC was completed by electron structure calculations confirming that it could be defined as a HR phase with a pronounced pseudogap at E_F in the DOS. However, the classical criterion based on the pseudogap would not be able to distinguish the thermodynamically most stable structure, which is an advantage of the proposed CDCCS instead.

This synergetic theoretical-experimental study indicates a way towards complex material design, urgently demanded by solid-state material scientists. In general, such a process consists of two steps: generation of candidate compounds and their quantum mechanical evaluation.

The use of graph theory to extract a set of Mackay approximants from accessible databases and the subsequent disclosure of key parameters from correlation diagrams (maps) may be integrated into a machine learning approach[77] to generate plausible new ACs. These outputs can be the starting point for a fine tuning of the disorder by CDCCS, which screen structure models in a small compositional range and discriminate them based on thermodynamics (evaluation step). Different types of structural disorder that are common for other ACs (*e.g.* the disordered inner tetrahedron for Tsai-type) could eventually be addressed in a similar way.

ACKNOWLEDGMENTS

The authors greatly acknowledge hardware and software facilities of the '*Zeolite*' supercomputer at the Samara Center for Theoretical Materials Science and the '*HybriLIT*' heterogeneous platform at the Laboratory of Information Technologies of the Joint Institute for Nuclear Research (Dubna, Russia). The study was partially funded by the Ministry of Science and Higher Education of the Russian Federation (project no. 3.6588.2017/9.10) and Russian Foundation for Basic Research (projects no. 18-03-00443). D. M. P. thanks the Università degli Studi di Milano for the

transition grants PSR2015-1718. TL thanks David Palmer for his ever-kind support with CrystalMakerX.

ASSOCIATED CONTENT

Supporting Information. Results of metallographic and DTA studies of prepared alloys; Sc-rich part of the Sc–Pd phase diagram adopted from the literature; ADPs anomalies for $Sc_{56}Pd_{15}$ ordered model from ISAM refinement; Tables containing selected experimental/structure determination parameters for studied crystals as well as comparison between ISAM, MEM and DFT data for *crystal II*; A list of Sc-rich ACs discovered up to date and their principal topological characteristics; the (001) ED plane recovered from MEM passing through the center of Mackay nanocluster overlaid with the edges of the individual cluster shells; QTAIM studies results showing the linear fitting trends of Bader volumes *vs*. Q_{eff} values for all the atoms together with Bader basins within the 1st icosahedral shell for Sc5, Sc1 and Sc4 species; Detailed description of single as well as combined point defect compositional/configurational space sampling; DFT relaxed, standardized structural data for the most energetically favorable $Sc_{55}Pd_{16}$ configuration; point density maps representing the selected Mackay-type ACs distribution as a function of average number of valence electrons per atom $(e/a)_{AC}$, electronegativity difference $\Delta\overline{\chi}$, and effective atomic size $R_{r.e}$; separate files containing the list of intermetallics containing Mackay cluster as a building unit, list of Mackay-type rational ACs discovered up to date, complete sets of the values of total energies, formation energies, and E_{hull} values corresponding both to the Sc_2Pd–$Sc_{56}Pd_{15}$–Sc and to the refined Sc_2Pd–$Sc_{55}Pd_{16}$–Sc convex hulls. This material is available free of charge via the Internet at http://pubs.acs.org.

AUTHOR INFORMATION

Corresponding Author

* pavlo.solokha@unige.it

ORCID

Pavlo Solokha: 0000-0002-5252-635X

Roman Eremin: 0000-0002-2550-9239

Tilmann Leisegang: 0000-0003-0386-3365

Davide Proserpio: 0000-0001-6597-9406

Tatiana Akhmetshina: 0000-0002-4124-6256

Albina Gurskaya: 0000-0003-2543-4932

Adriana Saccone: 0000-0002-0949-8859

Serena De Negri: 0000-0002-5345-8694

Author Contributions

The manuscript was written through contributions of all authors. All authors have given approval to the final version of the manuscript.

ABBREVIATIONS

AC, approximant; ADP, anisotropic thermal displacement parameter; CDCCS, combined defect compositional/configurational space; CIMs, complex intermetallics; ED, electron density; HR, Hume-Rothery; iQC, icosahedral quasicrystal; ISAM, independent spherical atom model; MEM, maximum entropy method; QTAIM, qantum theory of atoms in molecules; SDCCS, single defect compositional/configurational space.

REFERENCES

(1) Dshemuchadse, J.; Steurer, W. More Statistics on Intermetallic Compounds – Ternary Phases. *Acta Crystallogr. Sect. A* **2015**, *71* (3), 335–345. https://doi.org/10.1107/S2053273315004064.

(2) Samson, S. Crystal Structure of $NaCd_2$. *Nature* **1962**, *195* (4838), 259–262. https://doi.org/10.1038/195259a0.

(3) Samson, S. The Crsytal Structure of the Phase β Mg_2Al_3. *Acta Crystallogr.* **1965**, *19* (3), 401–413. https://doi.org/10.1107/S0365110X65005133.

(4) Weber, T.; Dshemuchadse, J.; Kobas, M.; Conrad, M.; Harbrecht, B.; Steurer, W. Large, Larger, Largest – a Family of Cluster-Based Tantalum Copper Aluminides with Giant Unit Cells. I. Structure Solution and Refinement. *Acta Crystallogr. Sect. B Struct. Sci.* **2009**, *65* (3), 308–317. https://doi.org/10.1107/S0108768109014001.

(5) Conrad, M.; Harbrecht, B.; Weber, T.; Jung, D. Y.; Steurer, W. Large, Larger, Largest – a Family of Cluster-Based Tantalum Copper Aluminides with Giant Unit Cells. II. The Cluster Structure. *Acta Crystallogr. Sect. B Struct. Sci.* **2009**, *65* (3), 318–325. https://doi.org/10.1107/S0108768109014013.

(6) Henley, C. L.; de Boissieu, M.; Steurer, W. Discussion on Clusters, Phasons and Quasicrystal Stabilisation. *Philos. Mag.* **2006**, *86* (6–8), 1131–1151. https://doi.org/10.1080/14786430500419395.

(7) Bergman, G.; Waugh, J. L. T.; Pauling, L. The Crystal Structure of the Metallic Phase $Mg_{32}(Al, Zn)_{49}$. *Acta Crystallogr.* **1957**, *10* (4), 254–259. https://doi.org/10.1107/S0365110X57000808.

(8) Takakura, H.; Gómez, C. P.; Yamamoto, A.; De Boissieu, M.; Tsai, A. P. Atomic Structure of the Binary Icosahedral Yb-Cd Quasicrystal. *Nat. Mater.* **2007**, *6* (1), 58–63. https://doi.org/10.1038/nmat1799.

(9) Mackay, A. L. A Dense Non-Crystallographic Packing of Equal Spheres. *Acta Crystallogr.* **1962**, *15* (9), 916–918. https://doi.org/10.1107/S0365110X6200239X.

(10) Tsai, A.-P. Discovery of Stable Icosahedral Quasicrystals: Progress in Understanding Structure and Properties. *Chem. Soc. Rev.* **2013**, *42* (12), 5352. https://doi.org/10.1039/c3cs35388e.

(11) Taylor, J.; Teich, E.; Damasceno, P.; Kallus, Y.; Senechal, M. On the Form and Growth of Complex Crystals: The Case of Tsai-Type Clusters. *Symmetry (Basel).* **2017**, *9* (9), 188. https://doi.org/10.3390/sym9090188.

(12) Thiel, P. When All Pieces Fit Together. *Nat. Mater.* **2007**, *6* (1), 11–12. https://doi.org/10.1038/nmat1814.

(13) Makongo, J. P. A.; Prots, Y.; Burkhardt, U.; Niewa, R.; Kudla, C.; Kreiner, G. A Case Study of Complex Metallic Alloy Phases: Structure and Disorder Phenomena of Mg–Pd Compounds. *Philos. Mag.* **2006**, *86* (3–5), 427–433. https://doi.org/10.1080/14786430500269212.

(14) Solokha, P.; De Negri, S.; Pavlyuk, V.; Eck, B.; Dronskowski, R.; Saccone, A. 3D [Ag-Mg] Polyanionic Frameworks in the $La_4Ag_{10}Mg_3$ and $La_4Ag_{10.3}Mg_{12}$ New Ternary Compounds. *J. Solid State Chem.* **2010**, *183* (12), 2995–3001. https://doi.org/10.1016/j.jssc.2010.10.018.

(15) De Negri, S.; Solokha, P.; Pavlyuk, V.; Saccone, A. The Isothermal Section of the La-Ag-Mg Phase Diagram at 400 °C. *Intermetallics* **2011**, *19* (5), 671–681. https://doi.org/10.1016/j.intermet.2011.01.007.

(16) Solokha, P.; De Negri, S.; Pavlyuk, V.; Saccone, A.; Fadda, G.

Synthesis and Crystallochemical Characterisation of the Intermetallic Phases $La(Ag_xMg_{1-x})_{12}$ ($0.11 \le x \le 0.21$), $LaAg_{4+x}Mg_{2-x}$ ($-0.15 \le x \le 1.05$) and $LaAg_{2+x}Mg_{2-x}$ ($0 < x \le 0.45$). *Eur. J. Inorg. Chem.* **2012**, *2012* (30), 4811–4821. https://doi.org/10.1002/ejic.201200700.

(17) Leisegang, T.; Meyer, D.; Doert, T.; Zahn, G.; Weissbach, T.; Souptel, D.; Behr, G.; Paufler, P. Incommensurately Modulated $CeSi_{1.82}$. *Zeitschrift fur Krist.* **2005**, *220*, 128–134. https://doi.org/10.1524/zkri.220.2.128.59116.

(18) Solokha, P.; De Negri, S.; Proserpio, D. M.; Blatov, V. A.; Saccone, A. Vacancy Ordering as a Driving Factor for Structural Changes in Ternary Germanides: The New $R_2Zn_{1-x}Ge_6$ Series of Polar Intermetallics (R = Rare-Earth Metal). *Inorg. Chem.* **2015**, *54* (5), 2411–2424. https://doi.org/10.1021/ic5030313.

(19) Freccero, R.; Solokha, P.; Proserpio, D. M.; Saccone, A.; De Negri, S. A New Glance on R_2MGe_6 (R = Rare Earth Metal, M = Another Metal) Compounds. An Experimental and Theoretical Study of R_2PdGe_6 Germanides. *Dalt. Trans.* **2017**, *46* (40), 14021–14033. https://doi.org/10.1039/c7dt02686b.

(20) Solokha, P.; Freccero, R.; De Negri, S.; Proserpio, D. M.; Saccone, A. The $R_2Pd_3Ge_5$ (R = La–Nd, Sm) Germanides: Synthesis, Crystal Structure and Symmetry Reduction. *Struct. Chem.* **2016**, *27* (6), 1693–1701. https://doi.org/10.1007/s11224-016-0812-z.

(21) Weissbach, T.; Leisegang, T.; Kreyssig, A.; Frontzek, M.; Hoffmann, J.-U.; Souptel, D.; Köhler, A.; Behr, G.; Paufler, P.; Meyer, D. Intergrowth of Several Solid Phases from the Y-Ni-B-C System in a Large YNi_2B_2C Crystal. *J. Appl. Crystallogr.* **2008**, *41*. https://doi.org/10.1107/S002188980801279X.

(22) Tang, F. Crystallographic Superstructure in R_2PdSi_3 Compounds (R=heavy Rare Earth). *Phys. Rev. B* **2011**, *84*, 104105.

(23) Zhu, Q.; Oganov, A. R.; Zhou, X.-F.; Zhu, Q.; Oganov, A. R.; Zhou, X.-F. Crystal Structure Prediction and Its Application in Earth and Materials Sciences. *Top Curr Chem* **2014**. https://doi.org/10.1007/128_2013_508.

(24) Trimarchi, G. Crystal Structure Prediction in the Context of Inverse Materials Design. *J. Semicond.* **2018**, *39* (7), 071004. https://doi.org/10.1088/1674-4926/39/7/071004.

(25) Blatov, B. Search for Isotypism in Crystal Structures by Means of the Graph Theory. *Acta Crystallogr. A.* **2000**, *56 (Pt 2)*, 178–188. https://doi.org/10.1107/S0108767399015512.

(26) Blatov, V. A.; Proserpio, D. M. Periodic-Graph Approaches in Crystal Structure Prediction. In *Modern Methods of Crystal Structure Prediction*; 2010; pp 1–28. https://doi.org/10.1002/9783527632831.ch1.

(27) Blatov, V. A. Crystal Structures of Inorganic Oxoacid Salts Perceived as Cation Arrays: A Periodic-Graph Approach. In *Structure and Bonding*; 2011; pp 31–66. https://doi.org/10.1007/430.

(28) Akhmetshina, T. G.; Blatov, V. A.; Proserpio, D. M.; Shevchenko, A. P. Topology of Intermetallic Structures: From Statistics to Rational Design. *Acc. Chem. Res.* **2018**, *51* (1), 21–30. https://doi.org/10.1021/acs.accounts.7b00466.

(29) Akhmetshina, T. G.; Blatov, V. A. A Fascinating Building Unit: Mackay Cluster in Intermetallics. *Struct. Chem.* **2017**, *28* (1), 133–140. https://doi.org/10.1007/s11224-016-0828-4.

(30) Blatov, V. A.; Shevchenko, A. P.; Proserpio, D. M. Applied Topological Analysis of Crystal Structures with the Program Package ToposPro. *Cryst. Growth Des.* **2014**, *14* (7), 3576–3586. https://doi.org/10.1021/cg500498k.

(31) Blatov *, V. A. Voronoi–Dirichlet Polyhedra in Crystal Chemistry: Theory and Applications. *Crystallogr. Rev.* **2004**, *10* (4), 249–318. https://doi.org/10.1080/08893110412331323170.

(32) Pankova, A. A.; Akhmetshina, T. G.; Blatov, V. A.; Proserpio, D. M. A Collection of Topological Types of Nanoclusters and Its Application to Icosahedron-Based Intermetallics. *Inorg. Chem.* **2015**, *54* (13), 6616–6630. https://doi.org/10.1021/acs.inorgchem.5b00960.

(33) O'Keeffe, M.; Peskov, M. A.; Ramsden, S. J.; Yaghi, O. M. The Reticular Chemistry Structure Resource (RCSR) Database of, and Symbols for, Crystal Nets. *Acc. Chem. Res.* **2008**, *41* (12), 1782–1789. https://doi.org/10.1021/ar800124u.

(34) Alexandrov, E. V.; Blatov, V. A.; Kochetkov, A. V.; Proserpio, D. M. Underlying Nets in Three-Periodic Coordination Polymers: Topology, Taxonomy and Prediction from a Computer-Aided Analysis of the Cambridge Structural Database. *CrystEngComm* **2011**, *13* (12), 3947. https://doi.org/10.1039/coce00636j.

(35) Okamoto, H. Pd-Sc (Palladium-Scandium). *J. Phase Equilibria* **2002**, *23* (6), 554–554. https://doi.org/10.1361/105497102770331334.

(36) Bruker. APEX2, SAINT-Plus, XPREP, SADABS, CELL_NOW and TWINABS. Inc., Bruker AXS: Madison, WI, USA 2014.

(37) Müller, P.; Herbst-Irmer, R.; L. Spek, A.; R. Schneider, T.; R. Sawaya, M. *Crystal Structure Refinement : A Crystallographers Guide to SHELXL*; Müller, P., Ed.; Oxford University Press: Oxford, UK, 2006.

(38) Farrugia, L. J.; IUCr. WinGX and ORTEP for Windows : An Update. *J. Appl. Crystallogr.* **2012**, *45* (4), 849–854. https://doi.org/10.1107/S0021889812029111.

(39) van Smaalen, S.; Palatinus, L.; Schneider, M. The Maximum-Entropy Method in Superspace. *Acta Crystallogr. Sect. A Found. Crystallogr.* **2003**, *59* (5), 459–469. https://doi.org/10.1107/S010876730301434X.

(40) Petříček, V.; Dušek, M.; Palatinus, L. Crystallographic Computing System JANA2006: General Features. *Zeitschrift für Krist. - Cryst. Mater.* **2014**, *229* (5). https://doi.org/10.1515/zkri-2014-1737.

(41) Bader, R. F. W. *Atoms in Molecules : A Quantum Theory*; Clarendon Press Oxford, 1990.

(42) Okhotnikov, K.; Charpentier, T.; Cadars, S. Supercell Program: A Combinatorial Structure-Generation Approach for the Local-Level Modeling of Atomic Substitutions and Partial Occupancies in Crystals. *J. Cheminform.* **2016**, *8* (1), 17. https://doi.org/10.1186/s13321-016-0129-3.

(43) Cenzual, K.; Chabot, B.; Parthé, E. Cubic $Sc_{57}Rh_{13}$ and Orthorhombic $Hf_{54}Os_{17}$, Two Geometrically Related Crystal Structures with Rhodium- and Osmium-Centred Icosahedra. *Acta Crystallogr. Sect. C Cryst. Struct. Commun.* **1985**, *41* (3), 313–319. https://doi.org/10.1107/S0108270185003754.

(44) Kresse, G.; Furthmüller, J. Efficient Iterative Schemes for Ab Initio Total-Energy Calculations Using a Plane-Wave Basis Set. *Phys. Rev. B* **1996**, *54* (16), 11169–11186. https://doi.org/10.1103/PhysRevB.54.11169.

(45) Kresse, G.; Joubert, D. From Ultrasoft Pseudopotentials to the Projector Augmented-Wave Method. *Phys. Rev. B* **1999**, *59* (3), 1758–1775. https://doi.org/10.1103/PhysRevB.59.1758.

(46) Perdew, J. P.; Burke, K.; Ernzerhof, M. Generalized Gradient Approximation Made Simple. *Phys. Rev. Lett.* **1996**, *77* (18), 3865–3868. https://doi.org/10.1103/PhysRevLett.77.3865.

(47) Hart, G. L. W.; Curtarolo, S.; Massalski, T. B.; Levy, O. Comprehensive Search for New Phases and Compounds in Binary Alloy Systems Based on Platinum-Group Metals, Using a Computational First-Principles Approach. *Phys. Rev. X* **2013**, *3* (4), 041035. https://doi.org/10.1103/PhysRevX.3.041035.

(48) Koepernik, K.; Eschrig, H. Full-Potential Nonorthogonal Local-Orbital Minimum-Basis Band-Structure Scheme. *Phys. Rev. B* **1999**, *59* (3), 1743–1757. https://doi.org/10.1103/PhysRevB.59.1743.

(49) Merlo, F.; Fornasini, M. L. Volume Effects in Rare Earth Intermetallic Compounds. *J. Alloys Compd.* **1993**, *197* (2), 213–

216. https://doi.org/10.1016/0925-8388(93)90043-M.
(50) Villars, P.; Daams, J. L. C. Atomic-Environment Classification of the Chemical Elements. *J. Alloys Compd.* **1993**, *197* (2), 177–196. https://doi.org/10.1016/0925-8388(93)90041-K.
(51) Mizutani, U.; Sato, H.; Mizutani, U.; Sato, H. The Physics of the Hume-Rothery Electron Concentration Rule. *Crystals* **2017**, *7* (1), 9. https://doi.org/10.3390/cryst7010009.
(52) Emsley, J. *The Elements*; Clarendon Press, 1998.
(53) Ferro, R.; Saccone, A. *Intermetallic Chemistry*; Elsevier, 2008.
(54) Rohrer, G. S. *Structure and Bonding in Crystalline Materials*; Cambridge University Press: Cambridge, 2001. https://doi.org/10.1017/CBO9780511816116.
(55) Gelato, L. M.; Parthé, E. STRUCTURE TIDY – a Computer Program to Standardize Crystal Structure Data. *J. Appl. Crystallogr.* **1987**, *20* (2), 139–143. https://doi.org/10.1107/S0021889887086965.
(56) Mizutani, U. *Hume-Rothery Rules for Structurally Complex Alloy Phases*; CRC Press, 2011.
(57) Gómez, C. P.; Lidin, S. Comparative Structural Study of the Disordered MCd_6 Quasicrystal Approximants. *Phys. Rev. B* **2003**, *68* (2), 024203. https://doi.org/10.1103/PhysRevB.68.024203.
(58) Gómez, C. P.; Tsai, A. P. Crystal Chemistry and Chemical Order in Ternary Quasicrystals and Approximants. *Comptes Rendus Phys.* **2014**, *15* (1), 30–39. https://doi.org/10.1016/j.crhy.2013.10.007.
(59) Walter, S.; Deloudi, S. *Crystallography of Quasicrystals*; Springer Series in Materials Science; Springer Berlin Heidelberg: Berlin, Heidelberg, 2009; Vol. 126. https://doi.org/10.1007/978-3-642-01899-2.
(60) Lin, Q.; Corbett, J. D. A Chemical Approach to the Discovery of Quasicrystals and Their Approximant Crystals. In *Controlled Assembly and Modification of Inorganic Systems*; Wu, X.-T., Ed.; Springer Berlin Heidelberg: Berlin, Heidelberg, 2009; pp 1–39. https://doi.org/10.1007/430_2008_11.
(61) Müller, P. *Crystal Structure Refinement : A Crystallographers Guide to SHELXL*; Oxford University Press, 2006.
(62) Lin, Q.; Corbett, J. D. New Building Blocks in the 2/1 Crystalline Approximant of a Bergman-Type Icosahedral Quasicrystal. *Proc. Natl. Acad. Sci.* **2006**, *103* (37), 13589–13594. https://doi.org/10.1073/pnas.0605954103.
(63) CrystalMakerX, Version 10.4.2. CrystalMaker Software Ltd. 2019.
(64) Mizutani, U.; Noritake, T.; Ohsuna, T.; Takeuchi, T. Hume-Rothery Electron Concentration Rule across a Whole Solid Solution Range in a Series of Gamma-Brasses in Cu–Zn, Cu–Cd, Cu–Al, Cu–Ga, Ni–Zn and Co–Zn Alloy Systems. *Philos. Mag.* **2010**, *90* (15), 1985–2008. https://doi.org/10.1080/14786430903246320.
(65) Mizutani, U.; Inukai, M.; Sato, H.; Zijlstra, E. Hume-Rothery Stabilization Mechanism and e/a Determination for RT- and MI-Type 1/1-1/1-1/1 Approximants Studied by FLAPW-Fourier Analyses. *Chem. Soc. Rev.* **2012**, *41*, 6799–6820. https://doi.org/10.1039/c2cs35161g.
(66) Mizutani, U.; Sato, H.; Inukai, M.; Zijlstra, E. S. Theoretical Foundation for the Hume-Rothery Electron Concentration Rule for Structurally Complex Alloys. *Acta Phys. Pol. A* **2014**, *126* (2), 531–534. https://doi.org/10.12693/APhysPolA.126.531.
(67) Steurer, W.; Dshemuchadse, J. *Intermetallics: Structures, Properties, and Statistics*; Oxford University Press, 2016. https://doi.org/10.1093/acprof:oso/9780198714552.001.0001.
(68) Lin, Q.; Corbett, J. D. Development of an Icosahedral Quasicrystal and Two Approximants in the Ca-Au-Sn System: Syntheses and Structural Analyses. *Inorg. Chem.* **2010**, *49* (22), 10436–10444. https://doi.org/10.1021/ic101356n.
(69) Lin, Q.; Corbett, J. D. Approximant Phases and an Icosahedral Quasicrystal in the Ca-Au-Ga System: The Influence of Size of Gallium versus Indium. *Inorg. Chem.* **2008**, *47* (17), 7651–7659. https://doi.org/10.1021/ic800694j.
(70) Graser, J.; Kauwe, S. K.; Sparks, T. D. Machine Learning and Energy Minimization Approaches for Crystal Structure Predictions: A Review and New Horizons. *Chem. Mater.* **2018**, *30* (11), 3601–3612. https://doi.org/10.1021/acs.chemmater.7b05304.
(71) Mizutani, U.; Sato, H.; Mizutani, U.; Sato, H. The Physics of the Hume-Rothery Electron Concentration Rule. *Crystals* **2017**, *7* (1), 9. https://doi.org/10.3390/cryst7010009.
(72) Müller, U. *Inorganic Structural Chemistry*; John Wiley & Sons, Ltd: Chichester, UK, 2006. https://doi.org/10.1002/9780470057278.
(73) Freccero, R.; Solokha, P.; De Negri, S.; Saccone, A.; Grin, Y.; Wagner, F. R. Polar-Covalent Bonding Beyond the Zintl Picture in Intermetallic Rare-Earth Germanides. *Chem. – A Eur. J.* **2019**, *25* (26), 6600–6612. https://doi.org/10.1002/chem.201900510.
(74) Kelton, K. F.; Lee, G. W.; Gangopadhyay, A. K.; Hyers, R. W.; Rathz, T. J.; Rogers, J. R.; Robinson, M. B.; Robinson, D. S. First X-Ray Scattering Studies on Electrostatically Levitated Metallic Liquids: Demonstrated Influence of Local Icosahedral Order on the Nucleation Barrier. *Phys. Rev. Lett.* **2003**, *90* (19), 195504. https://doi.org/10.1103/PhysRevLett.90.195504.
(75) An, S.; Li, J.; Li, Y.; Li, S.; Wang, Q.; Liu, B. Two-Step Crystal Growth Mechanism during Crystallization of an Undercooled $Ni_{50}Al_{50}$ Alloy. *Sci. Rep.* **2016**, *6* (1), 31062. https://doi.org/10.1038/srep31062.
(76) Kurtuldu, G.; Shamlaye, K. F.; Löffler, J. F. Metastable Quasicrystal-Induced Nucleation in a Bulk Glass-Forming Liquid. *Proc. Natl. Acad. Sci.* **2018**, *115* (24), 6123–6128. https://doi.org/10.1073/PNAS.1717941115.
(77) Eremin, R. A.; Zolotarev, P. N.; Golov, A. A.; Nekrasova, N. A.; Leisegang, T. Ionic Transport in Doped Solid Electrolytes by Means of DFT Modeling and ML Approaches: A Case Study of Ti-Doped $KFeO_2$. *J. Phys. Chem. C* **2019**, *123* (49), 29533–29542. https://doi.org/10.1021/acs.jpcc.9b07535.

Insert Table of Contents artwork here